Commun. Comput. Phys.
doi: 10.4208/cicp.OA-2023-0161

Vol. **35**, No. 1, pp. 181-211
January 2024

A Unified Gas-Kinetic Particle Method for Frequency-Dependent Radiative Transfer Equations with Isotropic Scattering Process on Unstructured Mesh

Yuan Hu[1], Chang Liu[1,*], Huayun Shen[1], Shiyang Zou[1] and Baolin Tian[1]

[1] *Institute of Applied Physics and Computational Mathematics, Beijing, China.*

Communicated by Kun Xu

Received 7 June 2023; Accepted (in revised version) 5 October 2023

Abstract. In this paper, we extend the unified gas kinetic particle (UGKP) method to the frequency-dependent radiative transfer equation with both absorption-emission and scattering processes. The extended UGKP method could capture the diffusion and free transport limit and provide a smooth transition in the physical and frequency space in the regime between the above two limits. The proposed scheme has the properties of asymptotic-preserving and regime-adaptive, which make it an accurate and efficient scheme in the simulation of multiscale photon transport problems. In the UGKP formulation of flux construction and distribution closure, the coefficients of the non-equilibrium free stream distribution and near-equilibrium Planck expansion are independent of the time step. Therefore, even with a large CFL number, the UGKP can preserve a physically consistent ratio of the non-equilibrium and the near-equilibrium proportion. The methodology of scheme construction is a coupled evolution of the macroscopic energy equation and the microscopic radiant intensity equation, where the numerical flux in the macroscopic energy equation and the closure in the microscopic radiant intensity equation are constructed based on the integral solution. Both numerical dissipation and computational complexity are well controlled, especially in the optically thick regime. 2D multi-thread code on a general unstructured mesh has been developed. Several numerical tests have been simulated to verify the numerical scheme and code, covering a wide range of flow regimes. The numerical scheme and code we developed are highly demanded and widely applicable in high-energy engineering applications.

AMS subject classifications: 65M08, 76P05, 82B40, 80A21

Key words: Frequency-dependent radiative transfer, multiscale method, asymptotic preserving, unified gas-kinetic particle method, unstructured mesh.

*Corresponding author. *Email addresses:* yuanhu@pku.org.cn (Y. Hu), liuchang@iapcm.ac.cn (C. Liu), shen_huayun@iapcm.ac.cn (H. Shen), zou_shiyang@iapcm.ac.cn (S. Zou), tian_baolin@iapcm.ac.cn (B. Tian)

1 Introduction

The thermal radiative transfer (TRT) equations, which describe the time evolution of radiative intensity and its interaction with the background material, have wide applications in astrophysics, atmospheric physics, inertial confinement fusion (ICF), high-temperature flow systems, plasma physics [1, 2], etc. It contains the kinetic radiation transport equation that describes the photon transport in the background material and the material energy equation that describes the energy exchange between radiation and background material. These two equations are coupled by the absorption-emission process that is characterized by the material opacity. The nonlinear dependency of the material opacity and material temperature makes the system difficult to solve [3, 4]. In addition, the high dimensionality of the equation greatly increases the computational cost. Developing numerical methods with high accuracy and high efficiency has become an important topic for the past decades.

Generally, the numerical methods for radiative transfer equations can be categorized into the deterministic method and the stochastic method. The deterministic methods include the macroscopic moment methods [5–10] and microscopic discrete ordinate SN method [11–15]. The moment methods propose a closure to the radiant intensity by expanding it in a specific functional space [16]. The SN methods directly discretize the velocity space using a specific quadrature. For stochastic methods, the most commonly used Monte Carlo (MC) method [17–20] exploits random numbers to simulate the interactions of individual radiation particles with the background material. The MC method is more efficient in optically thin regimes, especially for multi-dimensional cases, and does not suffer from the ray effect compared with the deterministic method. The implicit Monte Carlo (IMC) method proposed by Fleck and Cummings [17] is a popular Monte Carlo method for solving the TRT equations. This method approximates the rapid, dynamic timescale of photon absorption-emission processes via effective scattering events by the Fleck factor, according to which the nonlinear TRT equations are reformulated into a system of linearized equations and solved by the standard Monte Carlo method. However, it is generally noticed that the IMC method becomes inefficient in the optically thick region when the photon mean free path is much smaller than the flow characteristic length, and the particle collision becomes dominated. In such a regime, a great number of effective scattering events are calculated during a time step, which significantly increases the computational cost. Efforts have been made to improve the efficiency of the IMC method in optically thick regions [21, 22], such as the implicit Monte Carlo diffusion (IMD) [23], discrete diffusion Monte Carlo (DDMC) [24, 25] methods, as well as the moment-based scale-bridging method [26–30]. The IMD and DDMC methods are transport-diffusion hybrid methods that simulate the TRT equations with diffusion approximation in optically thick regions and the standard IMC method in other regions. For the transport-diffusion hybrid method, special efforts need to be made for the domain decomposition and the information exchange at transport-diffusion interfaces. For the moment-based scale-bridging method, coupled high-order and low-order

(HO-LO) equations are solved to improve the overall simulation efficiency for the TRT equations. Numerical principles such as the asymptotic-preserving property and the regime-adaptive property have been proposed to guide the multiscale numerical scheme construction [31–33].

The unified gas kinetic scheme (UGKS) has been constructed first to simulate both continuum, and rarefied flow [34], and then extended for the TRT problems [35–40]. The UGKS utilizes a finite volume formulation to solve the macroscopic transport and material energy equations, where the DOM method is employed to discretize the angle direction of the microscopic transport equation. In addition, the integral solution of the transport equation is employed to establish the time-dependent interface fluxes at a cell interface for both micro and macroscopic equations. This solution covers the physics from the free transport to the diffusion limit, which makes the UGKS asymptotic preserving (AP). Therefore, the UGKS accurately captures the diffusive and free transport solutions in optically thick and thin regimes respectively, as well as the solutions in the transition regime. Recently, the UGKS is extended to the particle-based Monte Carlo method, such as the unified gas kinetic particle (UGKP) [41, 42] and the unified gas-kinetic wave-particle (UGKWP) methods [43]. Similar to the UGKS framework, the UGKP and UGKWP methods employ a finite volume solver for the macroscopic transport and material energy equations and a particle-based Monte Carlo solver (instead of the DOM method) for the microscopic transport equation. Therefore, the UGKP and UGKWP methods have asymptotic preserving properties as well. In addition, the Monte Carlo solver has avoided the interdependence of complex polyhedral-mixed mesh in microscopic transport equation solving as in the DOM solver, which makes UGKP and UGKWP methods more suitable for problems with complex polyhedral-mixed mesh than UGKS method.

In this work, we extended the UGKP method for the frequency-dependent radiative system considering both absorption-emission and scattering processes, and the scheme is formulated on a general unstructured mesh. The UGKP and UGKWP methods have the same framework, with the only difference in the source sampling (The UGKWP method only resamples free-streamed photons, instead of all photons as in UGKP). Thus, all following derivations in this work are also suitable for the UGKWP method. The key methodology of the construction of UGKP is first the coupling evolution of the macroscopic energy equation and microscopic radiant intensity equation, and second the multiscale numerical flux and closure derived from the integral solution. The multi-group formulation is used to discretize the frequency space, and a multi-dimensional formulation is used for flux construction at the cell interface. The photon particles are sampled and tracked from multiple sources, including photons in census, photons from boundary/initial condition, and the macroscopic emission and scattering sources. The proposed scheme is capable to capture the multiscale flow physics in both spatial and frequency space. With the inclusion of the scattering effect, the flow regimes are enriched, covering the optically thin ballistic regime, optically thick single-temperature diffusive regime, and optically thick two-temperature diffusive regime [44, 45]. The proposed

UGKP preserves all three regime solutions in their corresponding flow regimes. Especially, the UGKP converges to a nine-point scheme [39, 46] on a distorted quadrilateral mesh in the diffusive regime.

The rest of this paper is organized as follows. In Section 2, we briefly introduce the TRT equations. In Section 3, the proposed UGKP method for solving the frequency-dependent radiative equations with considered both absorption-emission and scattering processes on an unstructured mesh is presented. Section 4 discusses the numerical properties, including the asymptotic preserving property and the regime-adaptive property of UGKP. Numerical results are shown in Section 5 to verify the UGKP method and the program. The summary and future work are given in Section 6.

2 Frequency-dependent radiative transfer equations

The frequency-dependent radiative transfer equations describe the transport of radiation and its energy exchange with the material. Under the assumption of local thermal equilibrium (LTE), the time-dependent frequency-dependent radiative transfer equations in the absence of both external and internal sources can be written in the following scaled form:

$$\begin{cases} \dfrac{\varepsilon}{c}\dfrac{\partial I}{\partial t}+\vec{\Omega}\cdot\nabla I = L_a^{\varepsilon}\sigma_a\left(B(\nu,T)-I\right)+L_s^{\varepsilon}\sigma_s\left(\dfrac{1}{4\pi}\displaystyle\int_{4\pi} I d\vec{\Omega}-I\right), \\ C_V\dfrac{\partial T}{\partial t}\equiv\dfrac{\partial U_m}{\partial t}=\dfrac{L_a^{\varepsilon}\sigma_a}{\varepsilon}\displaystyle\int_{4\pi}\int_0^{\infty}(I-B(\nu,T))\,d\nu d\vec{\Omega}. \end{cases} \tag{2.1}$$

Here $I\left(t,\vec{r},\vec{\Omega},\nu\right)$ is the radiation intensity which depends on time t, spatial variable $\vec{r}$, angular variable $\vec{\Omega}$, frequency variable $\nu\in(0,+\infty)$, $T(t,\vec{r})$ is the material temperature, $\sigma_a(\vec{r},\nu,T)$ is the absorption coefficient, $\sigma_s(\vec{r},\nu,T)$ is the scattering coefficient, c is the speed of light, $\varepsilon>0$ is the Knudsen number, L_a^{ε} and L_s^{ε} are two parameters depending on ε, $U_m(\vec{r},t)$ is the material energy density, and $C_V>0$ is the heat capacity. In addition, the Planck function $B(\nu,T)$ is defined by

$$B(\nu,T)=\frac{2h\nu^3}{c^2}\frac{1}{e^{h\nu/kT}-1}, \tag{2.2}$$

where h is Planck's constant and k is Boltzmann's constant. The assumption of isotropic scattering is taken in this work.

The photon flow regimes are enriched when both absorption and scattering processes are considered in system (2.1). In the optically thin regime, the system (2.1) degenerates to the free-stream ballistic regime. In the optically thick regime, when the absorption process dominates, the system asymptotically converges to a single-temperature diffusion equation, and when the scattering process dominates, the system asymptotically converges to a two-temperature diffusion system. Specifically, with $L_a^{\varepsilon}=1/\varepsilon$ and $L_s^{\varepsilon}=\varepsilon$, the absorption process will be dominated as $\varepsilon\to 0$. The equilibrium state with equal radiation and material temperature will be obtained, and the radiant intensity converges

to the local Planckian distribution $I \to B(\nu,T)$. The material temperature T_0 satisfies the following diffusion equation:

$$\frac{\partial}{\partial t}U_m(T_0)+\frac{\partial}{\partial t}\left(aT_0^4\right)=\nabla\cdot\frac{1}{3\sigma_a}\nabla\left(acT_0^4\right), \tag{2.3}$$

where a is the radiation constant given by

$$a=\frac{8\pi k^4}{15h^3c^3}.$$

When $L_a^\varepsilon=\varepsilon$ and $L_s^\varepsilon=1/\varepsilon$, the scattering process will be dominated as $\varepsilon\to 0$, and the two-temperature regime will be approached. If we define radiation energy as $\rho=\int_{4\pi}Id\vec{\Omega}$, the radiation intensity goes to $I\to\rho/4\pi$, and the radiation energy and material temperature T stratify the following nonlinear two-temperature diffusion system:

$$\begin{cases}\dfrac{\partial\rho}{\partial t}-\nabla\cdot\dfrac{c}{3\sigma_s}\nabla\rho=c\sigma_a(4\pi B(\nu,T)-\rho),\\ C_V\dfrac{\partial T}{\partial t}\equiv\dfrac{\partial U_m}{\partial t}=\sigma_a\displaystyle\int_0^\infty(\rho-4\pi B(\nu,T))d\nu.\end{cases} \tag{2.4}$$

One important thing is that the numerical scheme we construct keeps a consistent asymptotic behavior for the radiative transfer system (2.1), which is referred to as the asymptotic preserving (AP) property of the scheme [31,33].

3 UGKP for frequency-dependent radiative transfer system

In this section, we present the UGKP method for the frequency-dependent radiative equations with both absorption-emission and scattering processes under the unstructured mesh.

3.1 Frequency space discretization

The frequency variable ν is discretized with the standard multi-group method. The continuous frequency space $(0,+\infty)$ is discretized into G frequency internals with frequency boundary $\left(\nu_{g-1/2},\nu_{g+1/2}\right)$, where $g=1,\cdots,G$, and $\nu_{1/2}=0,\nu_{G+1/2}=\infty$. With the multi-group discretization, we integrate the first equation in (2.1) over each frequency interval:

$$\begin{aligned}&\int_{\nu_{g-1/2}}^{\nu_{g+1/2}}\left(\frac{\varepsilon}{c}\frac{\partial I}{\partial t}+\vec{\Omega}\cdot\nabla I\right)d\nu\\ =&\int_{\nu_{g-1/2}}^{\nu_{g+1/2}}[L_a^\varepsilon\sigma_a(B(\nu,T)-I)]d\nu+\int_{\nu_{g-1/2}}^{\nu_{g+1/2}}\left[L_s^\varepsilon\sigma_s\left(\frac{1}{4\pi}\int_{4\pi}Id\vec{\Omega}-I\right)\right]d\nu.\end{aligned} \tag{3.1}$$

For Eq. (3.1), the radiation intensity and energy in different groups and the corresponding group opacities are given by

$$I_g = \int_{\nu_{g-1/2}}^{\nu_{g+1/2}} I\left(t,\vec{r},\vec{\Omega},\nu\right) d\nu, \quad \rho_g = \int_{4\pi} I_g d\vec{\Omega}, \tag{3.2}$$

and

$$\begin{aligned} &\sigma_{e,g} = \frac{\int_{\nu_{g-1/2}}^{\nu_{g+1/2}} \sigma_a B(\nu,T) d\nu}{\int_{\nu_{g-1/2}}^{\nu_{g+1/2}} B(\nu,T) d\nu}, \quad \sigma_{a,g} = \frac{\int_{\nu_{g-1/2}}^{\nu_{g+1/2}} \sigma_a I d\nu}{\int_{\nu_{g-1/2}}^{\nu_{g+1/2}} I d\nu}, \\ &\sigma_{so,g} = \frac{\int_{\nu_{g-1/2}}^{\nu_{g+1/2}} \sigma_s I d\nu}{\int_{\nu_{g-1/2}}^{\nu_{g+1/2}} I d\nu}, \quad \sigma_{si,g} = \frac{\int_{\nu_{g-1/2}}^{\nu_{g+1/2}} \sigma_s \left(\int_{4\pi} I d\vec{\Omega}\right) d\nu}{\int_{\nu_{g-1/2}}^{\nu_{g+1/2}} \left(\int_{4\pi} I d\vec{\Omega}\right) d\nu}. \end{aligned} \tag{3.3}$$

For the Planck function $B(\nu,T)$ on the right side of Eq. (3.1), it is also integrated over the frequency interval by

$$\phi_g = \int_{\nu_{g-1/2}}^{\nu_{g+1/2}} B(\nu,T) d\nu. \tag{3.4}$$

With these notations in (3.2), (3.3), and (3.4), Eq. (2.1) turns to an equivalent multi-group radiative transfer system

$$\begin{cases} \dfrac{\varepsilon}{c}\dfrac{\partial I_g}{\partial t} + \vec{\Omega}\cdot\nabla I_g = L_a^\varepsilon\left(\sigma_{e,g}\phi_g - \sigma_{a,g} I_g\right) + L_s^\varepsilon\left(\sigma_{si,g}\dfrac{\rho_g}{4\pi} - \sigma_{so,g} I_g\right), \\ C_V \dfrac{\partial T}{\partial t} \equiv \dfrac{\partial U_m}{\partial t} = \dfrac{L_a^\varepsilon}{\varepsilon}\displaystyle\sum_{g=1}^{G}\int_{4\pi}\left(\sigma_{a,g} I_g - \sigma_{e,g}\phi_g\right) d\vec{\Omega}. \end{cases} \tag{3.5}$$

Note that the absorption opacity $\sigma_{a,g}$, scattering-in opacity $\sigma_{si,g}$, and scattering-out opacity $\sigma_{so,g}$ in Eq. (3.5) is a weighted integration with the unclosed radiant intensity $I(t,\vec{r},\vec{\Omega},\nu)$. The unclosed function $I(t,\vec{r},\vec{\Omega},\nu)$ in the above opacity integration is approximated by the Planck function with radiation temperature T_r,

$$\sigma_{a,g} = \frac{\int_{\nu_{g-1/2}}^{\nu_{g+1/2}} \sigma_a B(\nu,T_r) d\nu}{\int_{\nu_{g-1/2}}^{\nu_{g+1/2}} B(\nu,T_r) d\nu}, \quad \sigma_{si,g} = \sigma_{so,g} = \frac{\int_{\nu_{g-1/2}}^{\nu_{g+1/2}} \sigma_s B(\nu,T_r) d\nu}{\int_{\nu_{g-1/2}}^{\nu_{g+1/2}} B(\nu,T_r) d\nu}, \tag{3.6}$$

where the radiant temperature is defined as

$$acT_r^4 = \int_{4\pi}\int_0^\infty I d\nu d\vec{\Omega} = \sum_{g=1}^{G}\rho_g. \tag{3.7}$$

Let $\sigma_{s,g} = \sigma_{si,g} = \sigma_{so,g}$ as the scattering opacity, and the system (3.5) turns to:

$$\begin{cases} \dfrac{\varepsilon}{c}\dfrac{\partial I_g}{\partial t} + \vec{\Omega}\cdot\nabla I_g = L_a^\varepsilon\left(\sigma_{e,g}\phi_g - \sigma_{a,g} I_g\right) + L_s^\varepsilon\sigma_{s,g}\left(\dfrac{\rho_g}{4\pi} - I_g\right), \\ C_V \dfrac{\partial T}{\partial t} \equiv \dfrac{\partial U_m}{\partial t} = \dfrac{L_a^\varepsilon}{\varepsilon}\displaystyle\sum_{g=1}^{G}\int_{4\pi}\left(\sigma_{a,g} I_g - \sigma_{e,g}\phi_g\right) d\vec{\Omega}. \end{cases} \tag{3.8}$$

The following macroscopic equations can be obtained by taking the angular integration of the radiation transport equation in (3.8)

$$\begin{cases} \dfrac{\varepsilon}{c}\dfrac{\partial \rho_g}{\partial t}+\nabla\cdot\left\langle \vec{\Omega} I_g\right\rangle = L_a^{\varepsilon}\left(4\pi\sigma_{e,g}\phi_g-\sigma_{a,g}\rho_g\right), \\ C_V\dfrac{\partial T}{\partial t}\equiv\dfrac{\partial U_m}{\partial t}=\dfrac{L_a^{\varepsilon}}{\varepsilon}\displaystyle\sum_{g=1}^{G}\left(\sigma_{a,g}\rho_g-4\pi\sigma_{e,g}\phi_g\right), \end{cases} \tag{3.9}$$

where $\left\langle \vec{\Omega} I_g\right\rangle=\int_{4\pi}\vec{\Omega} I_g d\vec{\Omega}$.

3.2 Spatial and time discretization

Under the multi-group framework, we will give the discretization of spatial and time variables on unstructured mesh here, based on the finite volume method. The formulas are presented in a two-dimensional Cartesian space. The angle direction is denoted by $\vec{\Omega}=(\mu,\xi)$ with $\mu=\sqrt{1-\zeta^2}\cos\theta$ and $\xi=\sqrt{1-\zeta^2}\sin\theta$, where $\zeta\in[-1,1]$ is the cosine value of the angle between the propagation direction $\vec{\Omega}$ and the z-axis, and $\theta\in[0,2\pi)$ is the angle between the projection vector of $\vec{\Omega}$ onto the xy-plane and the x-axis. Due to the symmetry of angular distribution in the two-dimensional Cartesian case, we only need to consider $\zeta>0$. The computational domain is discretized into the unstructured mesh as shown in Fig. 1. The mesh center $c_j=\left(x_j^c,y_j^c\right)$ is given by

$$\left(x_j^c,y_j^c\right)=\frac{1}{V_j}\int_{V_j}(x,y)dxdy. \tag{3.10}$$

The time is discretized by t_n with time step $\Delta t=t_{n+1}-t_n$. A conservative finite volume numerical scheme for the macroscopic equation (3.9) is of the form

$$\begin{cases} \rho_{j,g}^{n+1}=\rho_{j,g}^{n}-\dfrac{\Delta t}{V_j}\displaystyle\sum_k\Phi_{j,k,g}^{n+1}+\dfrac{c\Delta t L_a^{\varepsilon}}{\varepsilon}\left(2\pi\left(\sigma_{e,g}\right)_j^{n+1}\phi_{j,g}^{n+1}-\left(\sigma_{a,g}\right)_j^{n+1}\rho_{j,g}^{n+1}\right), \\ C_V\dfrac{T_j^{n+1}-T_j^n}{\Delta t}=\dfrac{L_a^{\varepsilon}}{\varepsilon}\displaystyle\sum_{g=1}^{G}\left(\left(\sigma_{a,g}\right)_j^{n+1}\rho_{j,g}^{n+1}-2\pi\left(\sigma_{e,g}\right)_j^{n+1}\phi_{j,g}^{n+1}\right), \end{cases} \tag{3.11}$$

where $\rho_{j,g}^{n+1}$, $\phi_{j,g}^{n+1}$, and T_j^{n+1} are the cell averaged value at time t_{n+1} in cell j, and $\Phi_{j,k,g}^{n+1}$ is the macroscopic fluxes across the cell edge k, which are defined as

$$\begin{aligned} \rho_{j,g}^{n+1}&=\frac{1}{V_j}\int_{V_j}\rho_g(t_{n+1},x,y)dxdy, \\ \phi_{j,g}^{n+1}&=\frac{1}{V_j}\int_{V_j}\phi_g(t_{n+1},x,y)dxdy, \\ \Phi_{j,k,g}^{n+1}&=\frac{cl_k}{\varepsilon\Delta t}\int_{t_n}^{t_{n+1}}\vec{n}_k\cdot\left\langle\vec{\Omega} I_g\right\rangle(t,p_{k,m})dt, \end{aligned} \tag{3.12}$$

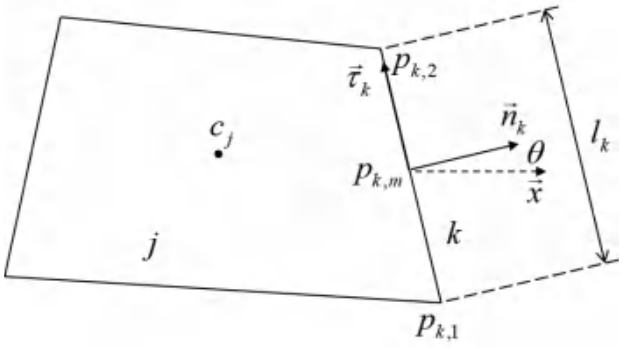

Figure 1: A cell j of the generalize quadrilateral mesh with c_j as the cell center, $p_{k,m}$ as the center of edge k. The length of the edge k is l_k. The tow vertexes of edge k are $\vec{p}_{k,1}$ and $\vec{p}_{k,2}$, and the unit normal and tangential vector is $\vec{n}_k$ and $\vec{\tau}_k$ respectively. θ is the angle between $\vec{n}_k$ and the x-axis.

where $p_{k,m}$ is the center of edge k, and $\vec{n}_k$ is the unit normal vector of edge k. The construction of $\Phi^{n+1}_{j,k,g}$ is the key to the UGKP method, which will be shown in the next subsection.

3.3 Construction of the macroscopic flux

The radiation intensity I_g around the center of edge k can be obtained by solving the following initial value problem

$$\begin{cases} \dfrac{\varepsilon}{c}\dfrac{\partial I_g}{\partial t}+\mu\dfrac{\partial I_g}{\partial x}+\xi\dfrac{\partial I_g}{\partial y}=L_a^{\varepsilon}\left(\sigma_{e,g}\phi_g-\sigma_{a,g}I_g\right)+L_s^{\varepsilon}\sigma_{s,g}\left(\dfrac{\rho_g}{2\pi}-I_g\right), \\ I_g(x,y,t)\big|_{t=t_n}=I_g(x,y,t_n). \end{cases} \tag{3.13}$$

On an unstructured mesh, we need to consider the flow variation in both normal and tangential directions ($\vec{n}_k$ and $\vec{\tau}_k$) at edge k. The angle between the normal direction $\vec{n}_k$ and the positive global x-axis $\vec{x}$ is θ, as shown in Fig. 1. The local coordinates follow

$$\begin{cases} \vec{n}_k=(\cos\theta,\sin\theta), \\ \vec{\tau}_k=(-\sin\theta,\cos\theta). \end{cases} \tag{3.14}$$

The transformation between the global coordinate (x,y) and local orthogonal coordinate (x',y') is

$$\begin{cases} x'=\left(x-x_j^{k,m}\right)\cos\theta+\left(y-y_j^{k,m}\right)\sin\theta, \\ y'=-\left(x-x_j^{k,m}\right)\sin\theta+\left(y-y_j^{k,m}\right)\cos\theta, \end{cases} \tag{3.15}$$

where $x_j^{k,m}$ and $y_j^{k,m}$ is the global coordinate of the edge center $p_{k,m}$. Then Eq. (3.13) can be written as

$$\begin{cases} \dfrac{\varepsilon}{c}\dfrac{\partial I_g}{\partial t}+\mu'\dfrac{\partial I_g}{\partial x'}+\xi'\dfrac{\partial I_g}{\partial y'}=L_a^{\varepsilon}\left(\sigma_{e,g}\phi_g-\sigma_{a,g}I_g\right)+L_s^{\varepsilon}\sigma_{s,g}\left(\dfrac{\rho_g}{2\pi}-I_g\right), \\ I_g\left(x',y',t\right)\big|_{t=t_n}=I_g\left(x',y',t_n\right), \end{cases} \tag{3.16}$$

where the transformation between (μ',ξ') and (μ,ξ) is similar to Eq. (3.15). With Eqs. (3.15) and (3.16), the integral solution can be obtained at the edge center $p_{k,m}$,

$$\begin{aligned} I_g(t,0,0)=&e^{-\lambda_g(t-t_n)}I_g\left(t_n,-\frac{\mu' c}{\varepsilon}(t-t_n),-\frac{\xi' c}{\varepsilon}(t-t_n)\right) \\ &+\int_{t_n}^{t}e^{-\lambda_g(t-s)}\left[\begin{array}{l}\frac{cL_a^{\varepsilon}\sigma_{e,g}}{\varepsilon}\phi_g\left(s,-\frac{\mu' c}{\varepsilon}(t-s),-\frac{\xi' c}{\varepsilon}(t-s)\right)\\ +\frac{cL_s^{\varepsilon}\sigma_{s,g}}{\varepsilon}\frac{\rho_g}{2\pi}\left(s,-\frac{\mu' c}{\varepsilon}(t-s),-\frac{\xi' c}{\varepsilon}(t-s)\right)\end{array}\right]ds, \end{aligned} \tag{3.17}$$

where $\lambda_g=c\left(L_a^{\varepsilon}\sigma_{a,g}+L_s^{\varepsilon}\sigma_{s,g}\right)/\varepsilon$. And the macroscopic flux across the edge k is evaluated by

$$\Phi_{j,k,g}^{n+1}=\frac{cl_k}{\varepsilon\Delta t}\int_{t_n}^{t_{n+1}}\left\langle\mu' I_g\right\rangle(t,0,0)\,dt. \tag{3.18}$$

The first term of Eq. (3.17) contributes from microscopic photons with free transport, including both the initial/boundary photons and the free photons from the previous time step in the computational domain. The second part of Eq. (3.17) denotes the contribution of macroscopic emission and scattering photons in this time step. Therefore, the integral solution (3.17) bridges the microscopic radiant flux and macroscopic diffusive flux, making (3.18) a multiscale numerical flux. The macroscopic quantities of Eq. (3.17) are reconstructed by a piecewise linear polynomial around the edge k as follows:

$$\begin{aligned} \phi_g\left(t,x',y'\right)&=\phi_{j,k,g}^{n+1}+\delta_t\phi_{j,k,g}^{n+1}(t-t_{n+1})+\delta_{y'}\phi_{j,k,g}^{n+1}y'+\delta_{x'}\phi_{j,k,g}^{n+1}x', \\ \rho_g\left(t,x',y'\right)&=\rho_{j,k,g}^{n+1}+\delta_t\rho_{j,k,g}^{n+1}(t-t_{n+1})+\delta_{y'}\rho_{j,k,g}^{n+1}y'+\delta_{x'}\rho_{j,k,g}^{n+1}x'. \end{aligned} \tag{3.19}$$

The spatial derivatives in (3.19) are calculated by

$$\begin{aligned} \delta_{x'}\phi_{j,k,g}^{n+1}&=\frac{\phi_{j',g}^{n+1}-\phi_{j,g}^{n+1}-\left(\tau_{j,k}^{-}+\tau_{j,k}^{+}\right)\left(\hat{\phi}_{k,2,g}^{n+1}-\hat{\phi}_{k,1,g}^{n+1}\right)}{l_{j,k}^{-}+l_{j,k}^{+}}, \quad \delta_{y'}\phi_{j,k,g}^{n+1}=\frac{\hat{\phi}_{k,2,g}^{n+1}-\hat{\phi}_{k,1,g}^{n+1}}{l_k}, \\ \delta_{x'}\rho_{j,k,g}^{n+1}&=\frac{\rho_{j',g}^{n+1}-\rho_{j,g}^{n+1}-\left(\tau_{j,k}^{-}+\tau_{j,k}^{+}\right)\left(\hat{\rho}_{k,2,g}^{n+1}-\hat{\rho}_{k,1,g}^{n+1}\right)}{l_{j,k}^{-}+l_{j,k}^{+}}, \quad \delta_{y'}\rho_{j,k,g}^{n+1}=\frac{\hat{\rho}_{k,2,g}^{n+1}-\hat{\rho}_{k,1,g}^{n+1}}{l_k}, \end{aligned} \tag{3.20}$$

where j' denotes the neighboring cell which has the common edge k with cell j. The $\hat{\phi}_{k,1,g}^{n+1}$, $\hat{\phi}_{k,2,g}^{n+1}$, and $\hat{\rho}_{k,1,g}^{n+1}$, $\hat{\rho}_{k,2,g}^{n+1}$ are the macroscopic quantities on the two vertexes ($p_{k,1}$ and $p_{k,2}$) of

edge k, which are calculated as the average macroscopic quantities of those cells that have the common vertex. The projected length is given by

$$\begin{cases} l_{j,k}^{-}=\vec{r}\left(c_j,p_{k,m}\right)\cdot\vec{n}_k, \\ l_{j,k}^{+}=\vec{r}\left(p_{k,m},c_{j'}\right)\cdot\vec{n}_k, \\ \tau_{j,k}^{-}=\left[\vec{r}\left(c_j,p_{k,m}\right)\cdot\vec{\tau}_k\right]/l_k, \\ \tau_{j,k}^{+}=\left[\vec{r}\left(p_{k,m},c_{j'}\right)\cdot\vec{\tau}_k\right]/l_k. \end{cases} \tag{3.21}$$

The time derivative in (3.19) is given by

$$\delta_t\phi_{j,k,g}^{n+1}=\frac{\phi_{j,k,g}^{n+1}-\phi_{j,k,g}^{n}}{\Delta t},\quad \delta_t\rho_{j,k,g}^{n+1}=\frac{\rho_{j,k,g}^{n+1}-\rho_{j,k,g}^{n}}{\Delta t}. \tag{3.22}$$

Based on the above reconstruction, the macroscopic interface flux $\Phi_{j,k,g}^{n+1}$ can be computed by substituting (3.17) into (3.18), which has the following form,

$$\begin{aligned} \Phi_{j,k,g}^{n+1}=&\left\langle \frac{cl_k}{\varepsilon\Delta t}\int_{t_n}^{t_{n+1}}\mu' e^{-\lambda_g(t-t_n)}I_g\left(t_n,-\frac{\mu' c}{\varepsilon}(t-t_n),-\frac{\xi' c}{\varepsilon}(t-t_n)\right)dt\right\rangle \\ &+\frac{2\pi}{3}\left(D^1\right)_{j,k,g}^{n+1}\delta_{x'}\phi_{j,k,g}^{n+1}+\frac{2\pi}{3}\left(D^2\right)_{j,k,g}^{n+1}\delta_{x'}\rho_{j,k,g}^{n+1}. \end{aligned} \tag{3.23}$$

The effective diffusion coefficients in (3.23) are given by

$$\begin{cases} D^1=-\dfrac{c^3 l_k L_a^{\varepsilon}\sigma_{e,g}}{\Delta t\varepsilon^3\lambda_g^2}\left[\Delta t\left(1+e^{-\lambda_g\Delta t}\right)-\dfrac{2}{\lambda_g}\left(1-e^{-\lambda_g\Delta t}\right)\right], \\ D^2=-\dfrac{c^3 l_k L_s^{\varepsilon}\sigma_{s,g}}{2\pi\Delta t\varepsilon^3\lambda_g^2}\left[\Delta t\left(1+e^{-\lambda_g\Delta t}\right)-\dfrac{2}{\lambda_g}\left(1-e^{-\lambda_g\Delta t}\right)\right]. \end{cases} \tag{3.24}$$

The expressions (3.24) have functional dependence on physical coefficients, the time step, and the asymptotic parameter:

$$\begin{aligned} \left(D^1\right)_{j,k,g}^{n+1}&=D^1\left(\Delta t,\varepsilon,\left(\sigma_{e,g}\right)_{j,k}^{n+1},\left(\lambda_g\right)_{j,k}^{n+1}\right), \\ \left(D^2\right)_{j,k,g}^{n+1}&=D^2\left(\Delta t,\varepsilon,\left(\sigma_{s,g}\right)_{j,k}^{n+1},\left(\lambda_g\right)_{j,k}^{n+1}\right), \end{aligned} \tag{3.25}$$

where the coefficients at the cell edge are the harmonic-averaged value with its neighboring cells. Similar to (3.17), Eq. (3.23) consists of a microscopic angular integral term and two macroscopic terms. The detailed formulation of macroscopic evolution will be shown in Subsection 3.4, and the microscopic evolution using the Monte Carlo method will be shown in Subsection 3.5.

3.4 Macroscopic solver for the radiation energy and material temperature

This subsection gives the UGKP macroscopic evolution algorithm with Eqs. (3.11), (3.17), and (3.23). The free-streaming fluxes (the integration term) in Eq. (3.23), calculated by the microscopic solver, will be discussed in Subsection 3.5. With calculated microscopic free-streaming fluxes, we could obtain a coupled nonlinear system for the macroscopic quantities T_j^{n+1} and $\rho_{j,g}^{n+1}$ by substituting (3.23) into the macroscopic equations (3.11). This nonlinear system is solved by a source iteration method.

Algorithm 1 Source iteration algorithm for macroscopic energy evolution.

1: Initialize flow field $\rho_{j,g}^{n+1,0}=\rho_{j,g}^{n}$ and $T_j^{n+1,0}=T_j^n$
2: **while** Residuals of $\rho_{j,g}^{n+1,s}$ and $T_j^{n+1,s}$ do not meet the convergence criterion **do**
3: Compute the coefficients $\left(\sigma_{e,g}\right)_j^{n+1,s}$, $\left(\sigma_{a,g}\right)_j^{n+1,s}$, $\left(D^1\right)_{j,k,g}^{n+1,s}$, $\left(D^2\right)_{j,k,g}^{n+1,s}$ with $T_j^{n+1,s}$.
4: Solve the inner-loop linear system to update $\rho_{j,g}^{n+1,s+1}$ and $T_j^{n+1,s+1}$ with

$$\begin{cases} \rho_{j,g}^{n+1,s+1}=\rho_{j,g}^{n}-\dfrac{\Delta t}{V_j}\sum\limits_k \Phi_{j,k,g}^{n+1,s}+\dfrac{c\Delta t L_a^{\varepsilon}}{\varepsilon}\left(2\pi\left(\sigma_{e,g}\right)_j^{n+1,s}\phi_{j,g}^{n+1,s+1}-\left(\sigma_{a,g}\right)_j^{n+1,s}\rho_{j,g}^{n+1,s+1}\right), \\ T_j^{n+1,s+1}=T_j^n+\dfrac{\Delta t L_a^{\varepsilon}}{\varepsilon C_V}\sum\limits_g\left(\left(\sigma_{a,g}\right)_j^{n+1,s}\rho_{j,g}^{n+1,s+1}-2\pi\left(\sigma_{e,g}\right)_j^{n+1,s}\phi_{j,g}^{n+1,s+1}\right), \\ \phi_{j,g}^{n+1,s+1}=\phi_{j,g}^{n+1,s}+\left(\dfrac{\partial\phi_g}{\partial T}\right)_j^{n+1,s}\left(T_j^{n+1,s+1}-T_j^{n+1,s}\right), \\ \dfrac{\partial\phi_g}{\partial T}=\int_{\nu_{g-1/2}}^{\nu_{g+1/2}}\dfrac{\partial B(\nu,T)}{\partial T}d\nu, \end{cases} \tag{3.26}$$

where the macroscopic flux $\Phi_{j,k,g}^{n+1,s}$ is given in (3.23)
5: **end while**
6: Update the solutions $\rho_{j,g}^{n+1}=\rho_{j,g}^{n+1,s+1}$ and $T_j^{n+1}=T_j^{n+1,s+1}$, and calculate $\phi_{j,g}^{n+1}$ through (3.4)

3.5 Microscopic solver for the radiation intensity

In this subsection, we present the Monte Carlo method for the microscopic evolution equation (3.16). The closure of the microscopic intensity of UGKP follows the first-order

expansion of the integral solution (3.17),

$$\begin{aligned}
I_g(t_{n+1},0,0) =& e^{-\lambda_g(t_{n+1}-t_n)} I_g\left(t_n,-\frac{\mu' c}{\varepsilon}(t_{n+1}-t_n),-\frac{\xi' c}{\varepsilon}(t_{n+1}-t_n)\right) \\
&+\int_{t_n}^{t_{n+1}} e^{-\lambda_g(t_{n+1}-s)} \left[\begin{array}{l} \frac{cL_a^\varepsilon\sigma_{e,g}}{\varepsilon}\phi_g\left(s,-\frac{\mu' c}{\varepsilon}(t_{n+1}-s),-\frac{\xi' c}{\varepsilon}(t_{n+1}-s)\right) \\ +\frac{cL_s^\varepsilon\sigma_{s,g}}{\varepsilon}\frac{\rho_g}{2\pi}\left(s,-\frac{\mu' c}{\varepsilon}(t_{n+1}-s),-\frac{\xi' c}{\varepsilon}(t_{n+1}-s)\right) \end{array}\right] ds \\
=& e^{-\lambda_g\Delta t} I_g\left(t_n,-\frac{\mu' c}{\varepsilon}\Delta t,-\frac{\xi' c}{\varepsilon}\Delta t\right) \\
&+\frac{1}{\lambda_g}\left(1-e^{-\lambda_g\Delta t}\right)\left[\frac{cL_a^\varepsilon\sigma_{e,g}}{\varepsilon}\phi_{j,g}^{n+1}+\frac{cL_s^\varepsilon\sigma_{s,g}}{\varepsilon}\frac{\rho_{j,g}^{n+1}}{2\pi}\right].
\end{aligned} \tag{3.27}$$

Once the macroscopic quantities $\rho_{j,g}^{n+1}$ and $\phi_{j,g}^{n+1}$ are obtained, we could recover the microscopic radiation intensity at t_{n+1}. In Eq. (3.27), there are three types of particles: the free-streaming particles from the previous time step $I_g(t_n)$, the re-emitted source $\phi_{j,g}^{n+1}$, and the scattered source $\rho_{j,g}^{n+1}\big/2\pi$. The particle free-streaming probability is $e^{-\lambda_g\Delta t}$, and the particle re-emission and scattering probability is $\left(1-e^{-\lambda_g\Delta t}\right)$. In addition, the factors $cL_a^\varepsilon\sigma_{e,g}\big/\lambda_g\varepsilon$ and $cL_s^\varepsilon\sigma_{s,g}\big/\lambda_g\varepsilon$ indicate the relative contribution of re-emission and scattering processes in the macroscopic source, depending on the corresponding cross sections. For the free-streaming particles, we stream them by its free path sampling from the total cross-section. For the re-emitted and scattered particles, we re-sample the photons as the second term in Eq. (3.27). The total energy of re-emitted and scattered photons are $\frac{1}{\lambda_g}\left(1-e^{-\lambda_g\Delta t}\right)\frac{cL_a^\varepsilon\sigma_{e,g}}{\varepsilon}\phi_{j,g}^{n+1}$ and $\frac{1}{\lambda_g}\left(1-e^{-\lambda_g\Delta t}\right)\frac{cL_s^\varepsilon\sigma_{s,g}}{\varepsilon}\frac{\rho_{j,g}^{n+1}}{2\pi}$, respectively. Then, the re-emitted and scattered photons are sampled in each mesh isotropically and uniformly.

The photon tracking algorithm in each time step is following. Three events should be calculated in each time step: (i) the photon interacts with background material and either be absorbed or be scattered; (ii) the photon exits the current cell and enters a cell with different opacity or leaks out of the system; (iii) the photon survives up to the end of the time step and goes to the census. Associated with the three events are three distances, i.e. the distance to collision d_C, the distance to the cell interface d_B, and the distance that would be traveled until the end of time step d_T. The calculation of each quantity is straightforward. The distance to collision d_C is sampled by

$$d_C = -\frac{1}{\sigma_t}\ln\chi, \tag{3.28}$$

where σ_t is the macroscopic total cross section of the medium in the current cell, and χ is a random number on $[0,1]$. The distance to the spatial cell interface d_B satisfies:

$$\vec{r}_B-\vec{r}=d_B\vec{\Omega}, \tag{3.29}$$

where $\vec{r}$ is the current location of each photon and $\vec{r}_B$ is the cell interface location in direction $\vec{\Omega}$. And the distance traveled to the end of time step is

$$d_t = c(t_{end} - t), \tag{3.30}$$

where t is the current time of each particle and t_{end} is the end of time step. With calculated distances in (3.28)-(3.30), the Monte Carlo solver determines which event to happen based on the minimum quantity of these three distances. The photon tracking in UGKP is similar to the traditional Monte Carlo method. Those photons with d_t as the minimum distance goes to census and will be further tracked in the next step. Those photons with d_B as the minimum distance will either go to a new mesh or leak out of the system (and be killed). The only difference between the microscopic solver of UGKP and the traditional Monte Carlo method is in the case with d_C as the minimum distance. Once the photon has "collided" with the material, the photon will be killed immediately. The subsequent behavior of these "collided" photons will be evaluated by the macroscopic solver of UGKP, instead of accurately tracking these photons in the traditional Monte Carlo method. During particle tracking, the net free-streaming flux in Eqs. (3.18) and (3.23) is obtained for photon i transports across the edge k, which is provided as the microscopic interface fluxes (the integration term) of Eq. (3.23) to close the macroscopic equations.

$$\Phi^{micro}_{j,k,g} = \sum_i \mathbb{1}(\Omega_{x'})(\vec{x}_i) w_{i,g}. \tag{3.31}$$

3.6 Summary

The coupled evolution of the macroscopic energy equation and microscopic intensity for the frequency-dependent radiative transfer system are presented in Subsections 3.4 and 3.5. We summarise the UGKP algorithm as follows, and the flowchart is given in Fig. 2.

Algorithm 2 The algorithm for UGKP method

1: Initialize the flow field and sample photon particles
2: **for** Simulation time less than the final time **do**
3: Stream all particles by their free path, and calculate the free-streaming flux
4: Apply the source iteration algorithm to evolve macroscopic field as in Subsection 3.4
5: Re-sample the re-emitted and scattered particles and close the microscopic intensity with Eq. (3.27)
6: **end for**

For the proposed UGKP method, the evolution of microscopic particles provides the free-streaming numerical flux for the macroscopic equations, and the solution of macroscopic equations provides the closure sources for the microscopic solver. The macro and microscopic evolution are closely coupled.

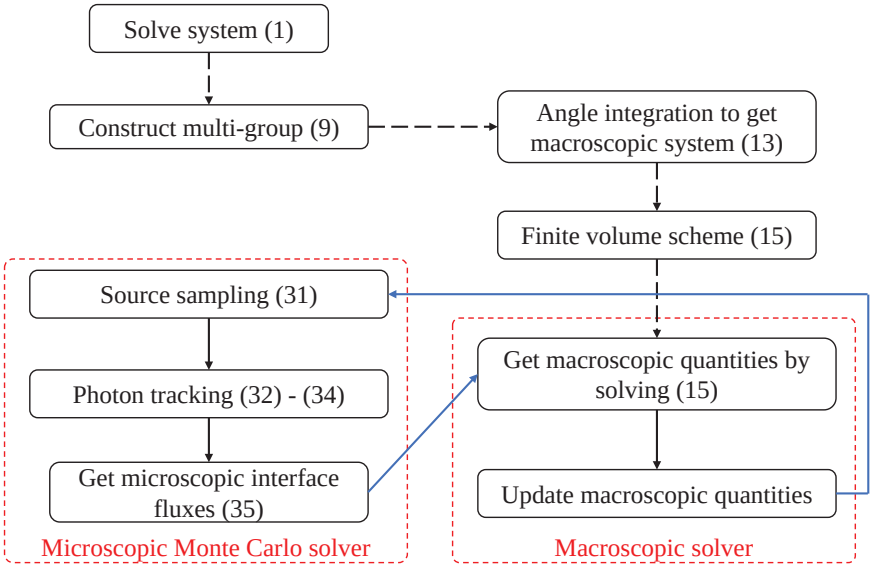

Figure 2: The flowchart of the UGKP method.

4 Asymptotic analysis

The asymptotic preserving (AP) property is important for the construction of a multiscale scheme. In this section, we will show that the proposed UGKP method preserves free transport, the single-temperature and the two-temperature diffusive regimes.

4.1 Free transport regime

In the free transport limit as σ_a and σ_s is on the order $\mathcal{O}(\sigma)\ll 1$, the coefficients in the macroscopic numerical flux (3.23) have the following asymptotic orders

$$\begin{aligned}
&\sigma_{e,g}\sim\mathcal{O}(\sigma),\quad \sigma_{a,g}\sim\mathcal{O}(\sigma),\quad \sigma_{s,g}\sim\mathcal{O}(\sigma),\\
&\lambda_g=c\left(\sigma_{a,g}+\sigma_{s,g}\right)\sim\mathcal{O}(\sigma),\quad e^{-\lambda_g(t-t_n)}\sim 1,\\
&\left(D^1\right)_{j,k,g}^{n+1}\sim-\frac{2c\left(\sigma_{e,g}\right)_{j,k}^{n+1}l_k}{\varepsilon^2\left[\left(\sigma_{a,g}\right)_{j,k}^{n+1}+\left(\sigma_{s,g}\right)_{j,k}^{n+1}\right]^2}\sim\mathcal{O}\left(\sigma^{-1}\right),\\
&\left(D^2\right)_{j,k,g}^{n+1}\sim-\frac{2c\left(\sigma_{s,g}\right)_{j,k}^{n+1}l_k}{2\pi\varepsilon^2\left[\left(\sigma_{a,g}\right)_{j,k}^{n+1}+\left(\sigma_{s,g}\right)_{j,k}^{n+1}\right]^2}\sim\mathcal{O}\left(\sigma^{-1}\right),
\end{aligned}\tag{4.1}$$

where L_a^ε and L_s^ε are taken as ε for simplicity. We apply asymptotic analysis to the macroscopic equation (3.11), and the $\mathcal{O}\left(\sigma^{-1}\right)$ equation is

$$\sum_k \frac{\phi_{j',g}^{n+1}-\phi_{j,g}^{n+1}-\left(\tau_{j,k}^-+\tau_{j,k}^+\right)\left(\hat{\phi}_{k,2}^{n+1}-\hat{\phi}_{k,1}^{n+1}\right)}{l_{j,k}^-+l_{j,k}^+}+\sum_k \frac{\rho_{j',g}^{n+1}-\rho_{j,g}^{n+1}-\left(\tau_{j,k}^-+\tau_{j,k}^+\right)\left(\hat{\rho}_{k,2}^{n+1}-\hat{\rho}_{k,1}^{n+1}\right)}{l_{j,k}^-+l_{j,k}^+}=0, \tag{4.2}$$

whose solution is

$$\phi_{j,g}^{n+1}=\phi_g^{n+1}, \quad \rho_{j,g}^{n+1}=\rho_g^{n+1}. \tag{4.3}$$

This means that the diffusive flux does not contribute to the evolution of the macroscopic quantities ϕ_g^{n+1} and ρ_g^{n+1}. Therefore, the macroscopic numerical flux (3.23) has the following form:

$$\Phi_{j,k,g}^{n+1}\to\left\langle \frac{cl_k}{\varepsilon\Delta t}\int_{t_n}^{t_{n+1}}\mu' I_g\left(t_n,-\frac{\mu' c}{\varepsilon}(t-t_n),-\frac{\xi' c}{\varepsilon}(t-t_n)\right)dt\right\rangle, \tag{4.4}$$

which indicates that the macroscopic numerical flux is the same as the tallied free transport flux of the microscopic Monte Carlo particles. The $\mathcal{O}\left(\sigma^0\right)$ equation is

$$\rho_{j,g}^{n+1}=\rho_{j,g}^n-\frac{\Delta t}{V_j}\sum_k\left\langle \frac{cl_k}{\varepsilon\Delta t}\int_{t_n}^{t_{n+1}}\mu' I_g\left(t_n,-\frac{\mu' c}{\varepsilon}(t-t_n),-\frac{\xi' c}{\varepsilon}(t-t_n)\right)dt\right\rangle, \tag{4.5}$$

which indicates that the radiation energy changes only because of the contribution of the tallied free transport flux of the microscopic Monte Carlo particles. Moreover, the $\mathcal{O}\left(\sigma^1\right)$ equation is

$$2\pi\phi_{j,g}^{n+1}-\rho_{j,g}^{n+1}=0 \tag{4.6}$$

which can be further deducted as

$$\sum_g 2\pi\phi_{j,g}^{n+1}=\sum_g\rho_{j,g}^{n+1}\ \Rightarrow\ \int_0^\infty\int_{2\pi}B(\nu,T)d\vec{\Omega}d\nu=\int_0^\infty\int_{2\pi}Id\vec{\Omega}d\nu\ \Rightarrow\ I=B(\nu,T). \tag{4.7}$$

This means that the system has reached the equilibrium state of free transport. The above analysis shows that the solution of the proposed UGKP method preserves the free transport solution in the free transport limit.

4.2 Single-temperature diffusion regime

For the single-temperature diffusion regime, or equilibrium diffusion limit, the Knudsen number ε approaches 0, $L_a^\varepsilon\sim 1/\varepsilon$, and $L_s^\varepsilon\sim\varepsilon$. The coefficients in the macroscopic numerical

flux (3.23) have the following orders

$$\begin{aligned}
&\lambda_g = \frac{c\left(\sigma_{a,g}/\varepsilon + \varepsilon\sigma_{s,g}\right)}{\varepsilon} \sim \mathcal{O}\left(\varepsilon^{-2}\right), \quad e^{-\lambda_g(t-t_n)} \to 0, \\
&\left(D^1\right)_{j,k,g}^{n+1} \to -\frac{c\left(\sigma_{e,g}\right)_{j,k}^{n+1} l_k}{\varepsilon^2\left[\left(\sigma_{a,g}\right)_{j,k}^{n+1}\Big/\varepsilon + \varepsilon\left(\sigma_{s,g}\right)_{j,k}^{n+1}\right]^2} \to -\frac{c\left(\sigma_{e,g}\right)_{j,k}^{n+1} l_k}{\left[\left(\sigma_{a,g}\right)_{j,k}^{n+1}\right]^2}, \\
&\left(D^2\right)_{j,k,g}^{n+1} \to -\frac{c\left(\sigma_{s,g}\right)_{j,k}^{n+1} l_k}{2\pi\left[\left(\sigma_{a,g}\right)_{j,k}^{n+1}\Big/\varepsilon + \varepsilon\left(\sigma_{s,g}\right)_{j,k}^{n+1}\right]^2} \sim \mathcal{O}\left(\varepsilon^2\right) \to 0.
\end{aligned} \tag{4.8}$$

Therefore, the macroscopic numerical flux (3.23) has the following form:

$$\Phi_{j,k,g}^{n+1} \to -\frac{2\pi}{3}\frac{c\left(\sigma_{e,g}\right)_{j,k}^{n+1} l_k}{\left[\left(\sigma_{a,g}\right)_{j,k}^{n+1}\right]^2}\delta_{x'}\phi_{j,k,g}^{n+1}. \tag{4.9}$$

Apply the asymptotic analysis to the macroscopic equations (3.11), and we have the $\mathcal{O}\left(\varepsilon^{-2}\right)$ equation

$$2\pi\left(\sigma_{e,g}\right)_j^{n+1}\phi_{j,g}^{n+1} - \left(\sigma_{a,g}\right)_j^{n+1}\rho_{j,g}^{n+1} = 0. \tag{4.10}$$

Sum over the group index g and we get

$$\int_0^\infty \int_{2\pi} \sigma_a B(\nu,T)\, d\vec{\Omega} d\nu = \int_0^\infty \int_{2\pi} \sigma_a I\, d\vec{\Omega} d\nu \tag{4.11}$$

which indicates that the leading order radiation temperature approaches the material temperature at the equilibrium limit

$$I = B(\nu,T) \Rightarrow 2\pi\phi_{j,g}^{n+1} = \rho_{j,g}^{n+1} \Rightarrow \left(\sigma_{e,g}\right)_j^{n+1} = \left(\sigma_{a,g}\right)_j^{n+1} = \left(\sigma_{P,g}\right)_j^{n+1}, \tag{4.12}$$

where $\sigma_{P,g}$ is the Planck mean opacity. Sum the macroscopic radiation transport equation over the group index g and coupled it with the material energy equation in (3.11), we derive the $\mathcal{O}\left(\varepsilon^0\right)$ equation

$$\begin{aligned}
\sum_{g=1}^{G}\rho_{j,g}^{n+1} = \sum_{g=1}^{G}\rho_{j,g}^{n} - \frac{\Delta t}{V_j}\sum_{g=1}^{G}\sum_k\left(-\frac{2\pi}{3}\frac{c l_k}{\left(\sigma_{P,g}\right)_{j,k}^{n+1}}\delta_{x'}\phi_{j,k,g}^{n+1}\right) \\
- cC_V\left(T_j^{n+1} - T_j^n\right).
\end{aligned} \tag{4.13}$$

According to Eq. (4.12), we have

$$\begin{cases}
\displaystyle\sum_g 2\pi\phi_{j,g}^{n+1} = \int_0^\infty \int_{2\pi} B\left(\nu, T_j^{n+1}\right) d\vec{\Omega} d\nu = ac\left(T_j^{n+1}\right)^4, \\
\displaystyle\sum_g \rho_{j,g}^{n+1} = \sum_g 2\pi\phi_{j,g}^{n+1} = ac\left(T_j^{n+1}\right)^4.
\end{cases} \tag{4.14}$$

It shows that Eq. (4.13) becomes a standard nine points scheme for the diffusion limit equation (2.3) coupled with (4.14). This shows that the proposed UGKP method for the frequency-dependent radiative transfer equations (2.1) preserves the single-temperature equilibrium diffusion limit.

4.3 Two-temperature diffusion regime

For the two-temperature diffusion regime or non-equilibrium diffusion limit, the Knudsen number ε approaches 0, $L_a^\varepsilon=\varepsilon$ and $L_s^\varepsilon=1/\varepsilon$. The coefficients in the macroscopic numerical flux (3.23) have the following orders

$$\begin{aligned}
&\lambda_g=\frac{c\left(\varepsilon\sigma_{a,g}+\sigma_{s,g}/\varepsilon\right)}{\varepsilon}\to o\left(\varepsilon^{-2}\right),\quad e^{-\lambda_g(t-t_n)}\to 0,\\
&\left(D^1\right)_{j,k,g}^{n+1}\to-\frac{c\left(\sigma_{e,g}\right)_{j,k}^{n+1}l_k}{\left[\varepsilon\left(\sigma_{a,g}\right)_{j,k}^{n+1}+\left(\sigma_{s,g}\right)_{j,k}^{n+1}/\varepsilon\right]^2}\to o\left(\varepsilon^2\right)\to 0,\\
&\left(D^2\right)_{j,k,g}^{n+1}\to-\frac{c\left(\sigma_{s,g}\right)_{j,k}^{n+1}l_k}{2\pi\varepsilon^2\left[\varepsilon\left(\sigma_{a,g}\right)_{j,k}^{n+1}+\left(\sigma_{s,g}\right)_{j,k}^{n+1}/\varepsilon\right]^2}\to-\frac{cl_k}{2\pi\left(\sigma_{s,g}\right)_{j,k}^{n+1}}.
\end{aligned}\tag{4.15}$$

The macroscopic numerical flux (3.23) has the following form:

$$\Phi_{j,k,g}^{n+1}\to-\frac{cl_k}{3\left(\sigma_{s,g}\right)_{j,k}^{n+1}}\delta_{x'}\rho_{j,k,g}^{n+1}.\tag{4.16}$$

Substituting the macroscopic numerical flux (4.16) into the macroscopic equations (3.11), and summing the macroscopic radiation transport equation over the group index g, we have

$$\begin{aligned}
\sum_{g=1}^{G}\rho_{j,g}^{n+1}=&\sum_{g=1}^{G}\rho_{j,g}^{n}-\frac{\Delta t}{V_j}\sum_{g=1}^{G}\sum_{k}\left(-\frac{cl_k}{3\left(\sigma_{s,g}\right)_{j,k}^{n+1}}\delta_{x'}\rho_{j,k,g}^{n+1}\right)\\
&+c\Delta t\sum_{g=1}^{G}\left(2\pi\left(\sigma_{e,g}\right)_j^{n+1}\phi_{j,g}^{n+1}-\left(\sigma_{a,g}\right)_j^{n+1}\rho_{j,g}^{n+1}\right)
\end{aligned}\tag{4.17}$$

Eq. (4.17) is a standard nine points scheme for the first diffusion limit equation in (2.4), independent of the parameter ε. The second equation of (2.4) is also independent of the parameter ε, and the convergence of Eq. (2.4) is automatically satisfied. This indicates that the proposed UGKP method for the frequency-dependent radiative transfer equations (2.1) preserves the two-temperature non-equilibrium diffusion limit.

5 Numerical examples

In this section, we present eight numerical examples to validate the extended UGKP method. These examples include two one-dimensional Marshak wave problems, the Tophat problem, a multi-group problem, two modified Marshak wave problems, and two wave diffusion problems. In the following computations, the unit of length is taken to be centimeter (cm), the mass unit is gram (g), the time unit is nanosecond (ns), the temperature unit is kilo electronvolt (keV), and the energy unit is 10^9 Joules (GJ). Under the above units, the speed of light is $29.98 cm/ns$, and the radiation constant a is $0.01372 GJ/(cm^3 keV^4)$.

5.1 Marshak wave-2A problem

First, we take the one-dimensional Marshak wave problems to verify the extended UGKP method. In the Marshak wave-2A problem, a thermal wave was driven by a constant intensity incident on the left boundary of the computational domain. The temperature of the left boundary source is 1 keV, while the initial material and radiation temperature are in equilibrium at 10^{-6} keV. The computational domain is a slab 1.0 cm thick which consists of an unstructured mesh with a maximum size of 0.005 cm. The absorption/emission coefficient is set to be temperature-dependent of $\sigma = 30.0/T^3 cm^{-1}$, and the specific heat to be $0.3 GJ/keV/cm^3$.

In Fig. 3(a), the material and radiation temperatures simulated using the UGKP method at times 0.2, 0.4, 0.6, 0.8, and 1.0 ns are given, compared with the reference results in [16]. The small absorption/emission coefficient violates the equilibrium diffusion approximation in this case. This violation can be observed in the comparison between the computed UGKP material temperatures, the diffusion equations results and the reference results in Fig. 3(b). These results show that the proposed scheme works well for this rarefied-to-transitional flow regime.

5.2 Marshak wave-2B problem

The Marshak wave-2B problem is the same as the Marshak wave-2A problem except that it has a temperature-dependent absorption/emission coefficient with $\sigma = 300.0/T^3 cm^{-1}$. With this absorption/emission coefficient, the flow regime covers the transitional to continuum flow regimes, and the solution converges to the diffusion limit solution.

The material and radiation temperatures simulated using the UGKP method at times 15, 30, 45, 60, and 74 ns are given in Fig. 4(a), compared with the reference results in [16]. In Fig. 4(b), the computed material temperatures for both UGKP simulation and diffusion equations results at times 15, 45, 74 ns are given, as well as the reference results. It is observed that the UGKP results are close to the diffusive limit results.

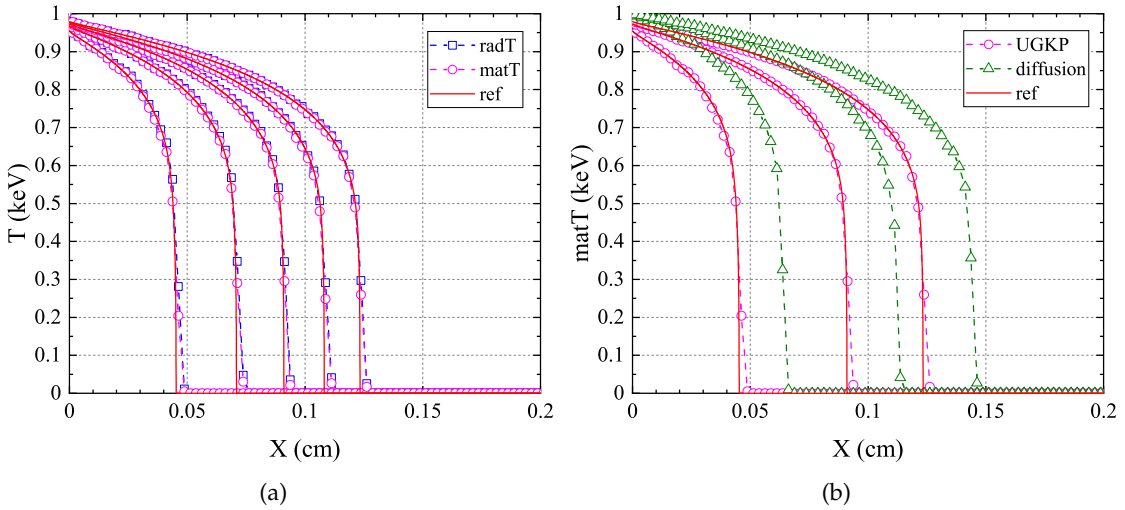

Figure 3: The results of Marshak wave-2A problem. (a) The radiation and material temperature at times 0.2, 0.4, 0.6, 0.8, and 1.0 ns, compared with the reference solutions. (b) The material temperature from UGKP simulation and the diffusion equation solution at time 0.2, 0.6, and 1.0 ns, compared with the reference solutions.

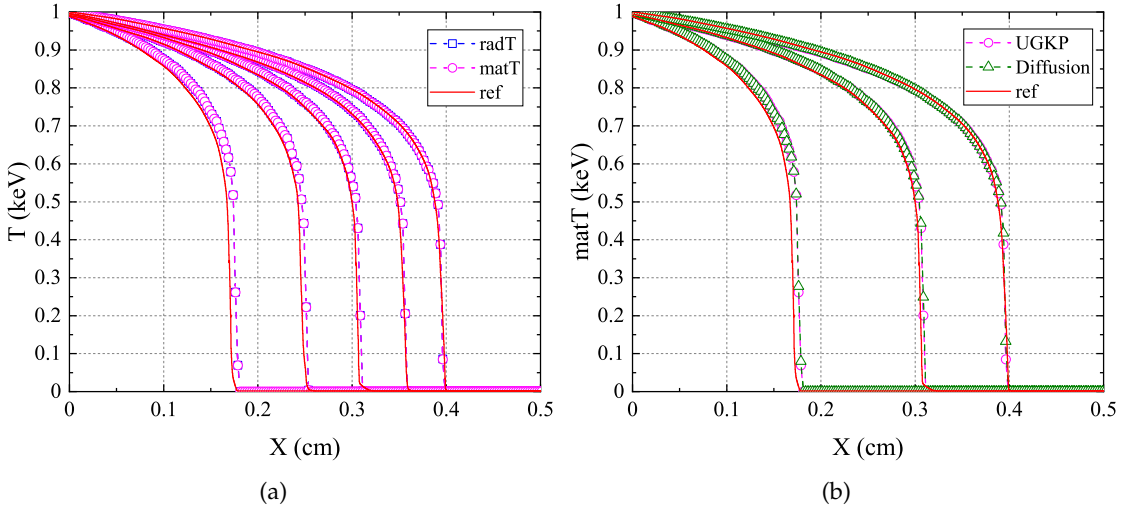

Figure 4: The results of Marshak wave-2B problem. (a) The radiation and material temperature at times 15, 30, 45, 60, and 74 ns, compared with the reference solutions. (b) The material temperature from UGKP simulation and the diffusion equation solution at time 15, 45, and 74 ns, compared with the reference solutions.

5.3 Tophat problem

The Tophat problem, or the crooked pipe problem, is a two-dimensional problem consisting of both optically thin and thick material. The size of the computational do-

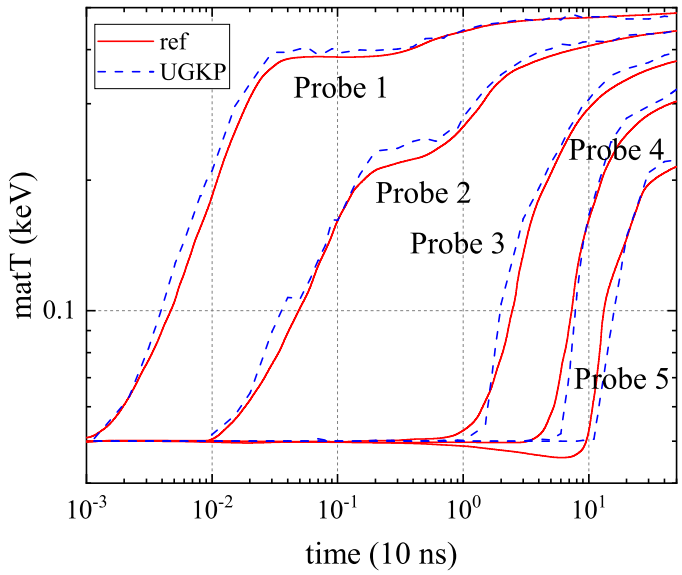

Figure 5: The material temperature over time for the five probes in the Tophat problem, compared with the reference solutions.

main is [0,7]×[-2,2], which consists of an unstructured mesh with a maximum size of 0.08 cm. The dense, opaque material with density $10g/cm^3$ and opacity $\sigma = 2000cm^{-1}$ is located in the regions $[3,4]\times[-1,1]$, $[0,2.5]\times[0.5,2]$, $[0,2.5]\times[-2,-0.5]$, $[4.5,7]\times[0.5,2]$, $[4.5,7]\times[-2,-0.5]$, $[2.5,4.5]\times[1.5,2]$, $[2.5,4.5]\times[-2,-1.5]$. And the optically thin material with density $0.01g/cm^3$ and opacity $\sigma = 0.2cm^{-1}$ occupies the other regions. The heat capacity is $0.1GJ/g/keV$ for both optically thin and thick materials. Initially, the system is in equilibrium at $0.05keV$, while a surface source at $0.5keV$ is located on the left boundary of the pipe for $-0.5 < y < 0.5$. In addition, five probes are used to track the temperature evolving in the pipe, placed at [0.25,0], [2.75,0], [3.5,1.25], [4.25,0], and [6.75,0].

The time-dependent material temperature for the five tracking probes is shown in Fig. 5, compared with the reference results in [47]. The material temperature over time simulated by the UGKP method is similar to the reference solution. In addition, Fig. 6(a)-(d) depict the material temperatures simulated by the UGKP method at 20, 80, 150, and 300 ns, respectively. It is shown that the interface between the optically thin and thick materials is captured sharply by the UGKP method.

5.4 Multi-group transport problem

As shown in the Marshak wave problems and the Tophat problem above, we have validated the extended UGKP method for the gray radiative transfer cases. The next example is a multi-group problem which we designed to test the extended UGKP method for the frequency-dependent radiative transfer cases. In this multi-group problem, we employ three frequency groups. The layout of this multi-group problem is shown in Fig. 7. The

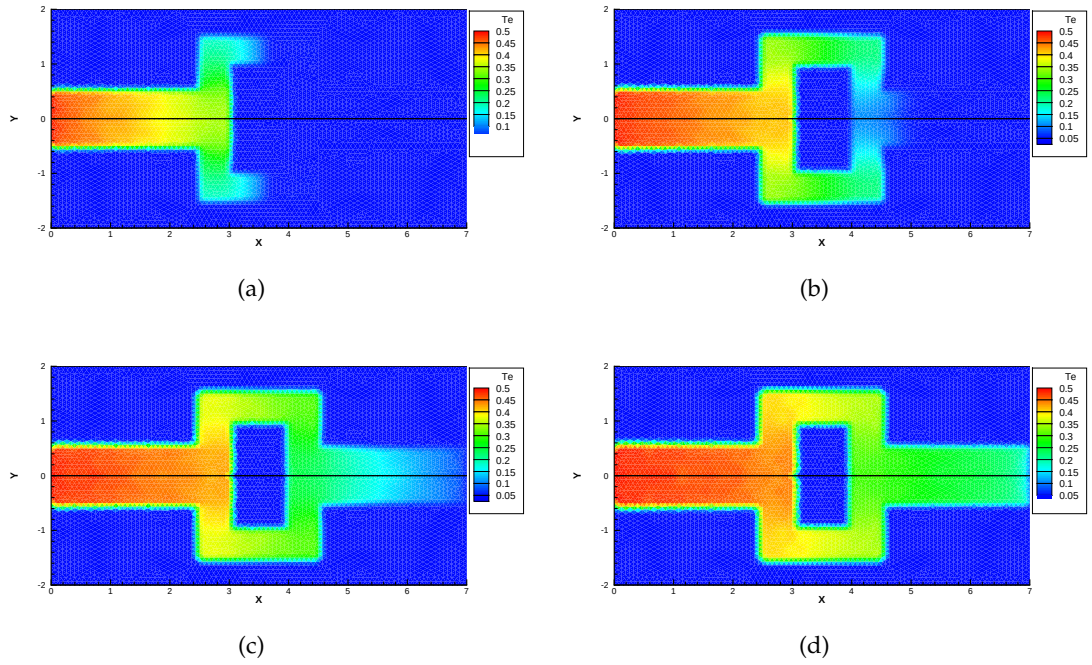

Figure 6: The material temperatures simulated by UGKP method at time (a) 20 ns, (b) 80 ns, (c) 150 ns, (d) 300 ns.

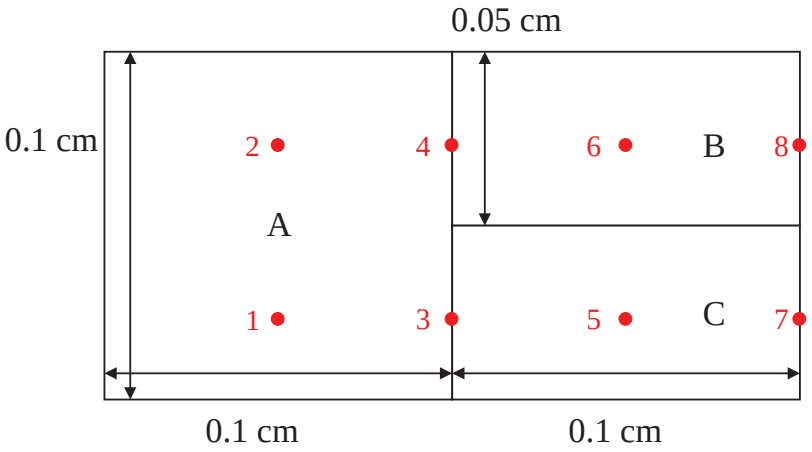

Figure 7: The layout of the multi-group problem.

size of the computational domain is $[0,0.2]\times[-0.05,0.05]$, which consists of an unstructured mesh with a maximum size of 0.02 cm. In addition, it consists of three zones: one frequency-independent zone (zone A) and two frequency-dependent zones (zone B and

Table 1: The opacity and specific heat for the 3 zones in the multi-group problem.

Zone	Specific heat ($GJ/keV/cm^3$)	Opacity G1 (cm^{-1})	Opacity G2 (cm^{-1})	Opacity G3 (cm^{-1})
A	0.01	10	10	10
B	0.2	1000	100	10
C	0.2	100	10	1000

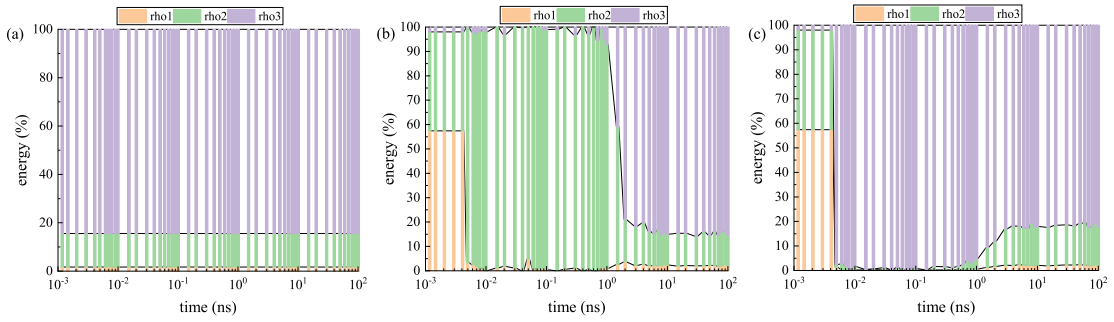

Figure 8: The radiation energy of three different frequency groups over time for (a) the left boundary source, (b) probe 5, (c) probe 6 in the multi-group problem.

C), with detailed opacity and specific heat listed in Table 1. The computational domain is initially in equilibrium at $0.05keV$, and a $0.5keV$ surface source with a Planck distribution is located on the left boundary. We also take eight probes to track the material temperature evolving in the different zone at different places, which are placed at $[-0.025,0.05]$, $[0.025,0.05]$, $[-0.025,0.1]$, $[0.025,0.1]$, $[-0.025,0.15]$, $[0.025,0.15]$, $[-0.025,0.2]$, $[-0.025,0.2]$. The location of these probes is also shown in Fig. 7.

To clearly show the difference between the radiation energy of different frequency groups transmitting over time, we compared the radiation energy at different places. First, the radiation energy of three frequency groups incident from the left boundary source is shown in Fig. 8(a). It can be seen that the input radiation energy is dominated by frequency group 3. Figs. 8(b) and 8(c) give the radiation energy changing over time at probe 5 and probe 6, respectively. In the beginning, the radiation energy of both probe 5 and probe 6 is dominated by frequency groups 1 and 2. With time increasing, the frequency group 2 becomes the leading group for probe 5, while the leading group changes into the frequency group 3 for probe 6. This difference is caused by the different opacities of frequency groups in zone B and C. Zone B has the smallest opacity for frequency group 3, which make frequency group 3 to be the leading group for probe 6. However, the frequency group with the smallest opacity changes into frequency group 2 for zone C, which also leads to a shift in the leading group. With time going on, the radiation energy of different frequency groups become similar to the input energy for both probe 5 and 6.

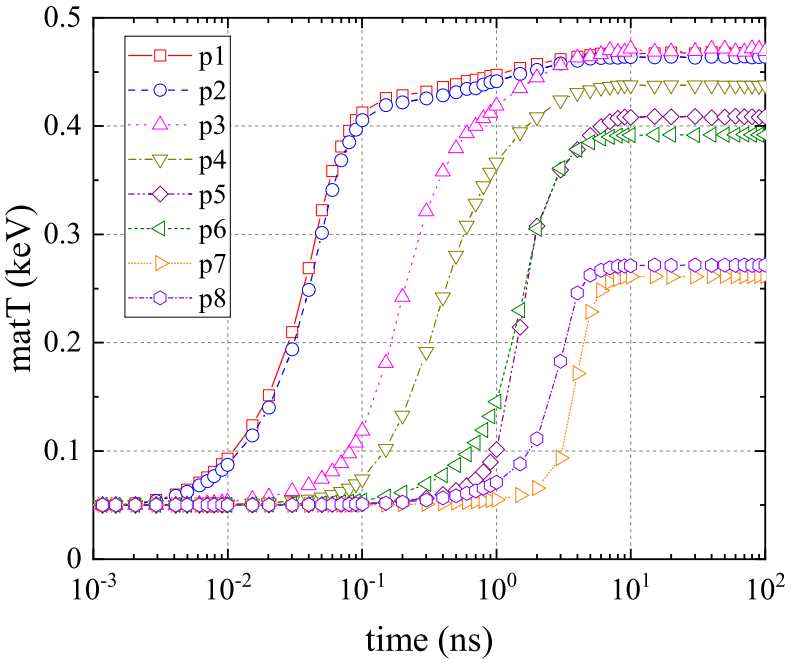

Figure 9: The material temperature over time for the eight probes in the multi-group problem.

We also compared the material temperature evolving at the eight probes, which are shown in Fig. 9. With frequency-independent opacity in zone A, the temperature is the same for probes 1 and 2. For probe 3, its material temperature is higher than probe 4, which is also caused by the different opacities of frequency groups on zone B and C. With the highest opacity for frequency group 3 in zone C, the input radiation energy (dominated by frequency group 3) is more likely to be deposited in zone C. However, the smallest opacity for frequency group 3 on zone B makes the input radiation energy unlikely to be absorbed by the material. Thus, the material temperature of probe 4 is smaller than probe 3. In addition, the more input energy deposited in zone C, the less input energy transmits in zone C, which makes the radiation transport in zone C slower than in zone B. This can be clearly seen by the material temperatures of probes 5, 6, 7, and 8 in Fig. 9. The material temperature of probe 5 is smaller than probe 6 during the radiation transport, and probes 7 and 8 have similar results. These results confirm the capability of the extended UGKP method for frequency-dependent radiative transfer cases.

5.5 Marshak wave-scatter problem

To further test the extended UGKP method for both absorption/emission and isotropic scattering processes considered cases, we include the scattering effect in the Marshak wave problems. The Marshak wave-scatter problem is similar as the Marhsak wave

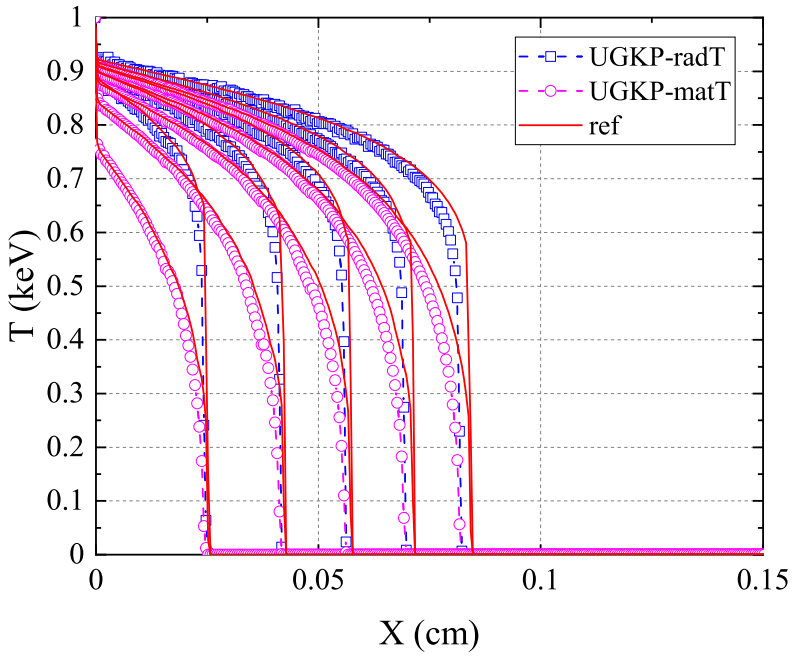

Figure 10: The results of Marshak wave-scatter problem. The radiation and material temperature at times 0.05, 0.1, 0.15, 0.2, and 0.25 ns, compared with the reference solutions.

problem, except that the temperature-dependent coefficient for both scattering and absorption/emission processes with $\sigma_s = 3.0/T^3 cm^{-1}$ are considered.

The material and radiation temperatures from the UGKP simulation for this problem is given in Fig. 10, as well as the reference results calculated by UGKS. The results of UGKP and UGKS have good agreement in general, while the slightly difference at wave front is due to the numerical dissipation of UGKS.

5.6 Marshak wave-2B-scatter problem

The modified Marshak wave-2B-scatter problem is the same as the Marhsak wave-2B problem, except that a temperature-dependent scattering coefficient with $\sigma_s = 300.0/T^3 cm^{-1}$ is considered. This also makes the total opacity in this problem twice as the Marhsak wave-2B problem.

Fig. 11(a) shows the material and radiation temperatures from UGKP simulation for this problem, compared with the reference results calculated by UGKS. Since the absorption/emission coefficient in Marshak wave-2B problem is large enough to get the equilibrium diffusion limit solution, twice the total opacity in this problem will also get the equilibrium diffusion limit solution. Therefore the UGKP results are also close to the diffusive limit results, as shown in Fig. 11(b). In addition, the radiation propagation speed for both UGKP simulation and the diffusion equation solution is also half as in the Mar-

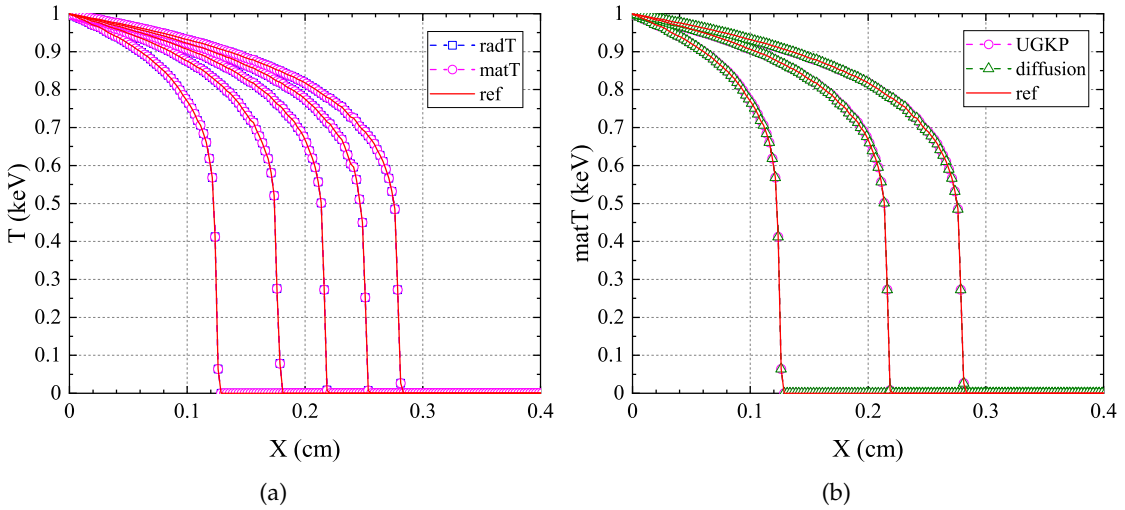

Figure 11: The results of Marshak wave-2B-scatter problem. (a) The radiation and material temperature at times 15, 30, 45, 60, and 74 ns, compared with the reference solutions. (b) The material temperature from UGKP simulation and the diffusion equation solution at time 15, 45, and 74 ns, compared with the reference solutions.

shak wave-2B problem, due to the twice total opacity in this problem. This can be seen by comparing Figs. 4 and 11. These results show that the proposed scheme works well for problem with both absorption/emission and isotropic scattering processes considered.

5.7 Sinusoidal wave diffusion problem

Next, we consider two wave diffusion problems with only scattering process, under one-dimensional space. In the first problem, the radiation energy ρ is taken as $\rho(x,t=0)=10+5cos\left(\frac{\pi}{2}x\right),x\in[-2,2]$, with periodic boundary conditions. In the diffusion limit, the time evolution of the amplitude follows:

$$\begin{cases}\delta\rho(x,t)=\rho(x,t)-10,\\ \dfrac{\partial}{\partial t}\delta\rho-D\dfrac{\partial^2}{\partial x^2}\delta\rho=0\end{cases}\Rightarrow A(x,t)=\delta\rho(x,t)=\cos\left(\frac{\pi}{2}x\right)e^{-D\left(\frac{\pi}{2}\right)^2t}. \tag{5.1}$$

In the following, we take the time evolution of amplitude at peak and valley location ($A(0,t)$ and $A(2,t)$, respectively) for comparison with the theory value in (5.1).

Fig. 12 gives the time evolution of amplitude at peak and valley location under different cross-section, compared with the theory value. For both $\sigma=100$ and $\sigma=1000$ cases, the UGKP simulated results show good agreements with the theory value. In addition, with the coefficient increasing, the flow regime covers the transitional to continuum flow regimes, and the solution also converges to the diffusion limit solution.

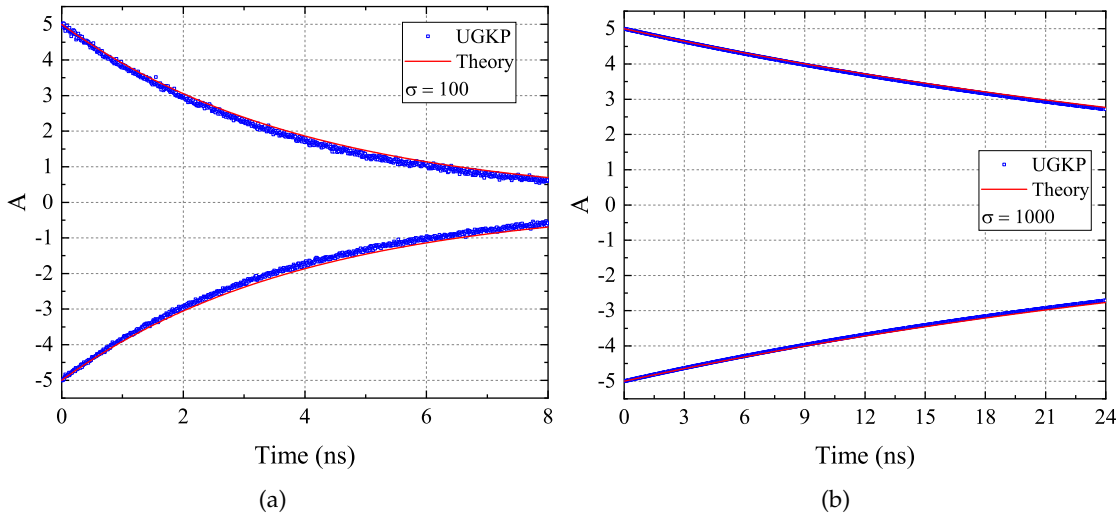

Figure 12: The time evolution of amplitude at peak and valley location for (a) $\sigma=100$, (b) $\sigma=1000$, compared with the theory value in (5.1).

5.8 Gauss wave diffusion problem

Besides the sinusoidal wave diffusion problem, we have also considered a Gauss wave diffusion problem. In this problem, the radiation energy ρ is taken as $\rho(x,t=0)=\delta(0)$. With this initial condition, the time evolution of the amplitude under the diffusion limit follows:

$$\begin{cases} \rho(x,t)=\dfrac{1}{2\pi}\displaystyle\int_{-\infty}^{\infty}\tilde{\rho}(k,t)e^{ikx}dk, \\ \dfrac{\partial}{\partial t}\rho-D\dfrac{\partial^2}{\partial x^2}\rho=0 \end{cases} \Rightarrow A(x,t)=\rho(x,t)=\left(\frac{1}{4\pi Dt}\right)^{1/2}e^{-\frac{x^2}{4Dt}}. \tag{5.2}$$

In the following, we take the initial simulation time as 1 ns, and compare both the time evolution of amplitude at $x=0$ and the distribution under different time with the theory value in (5.2), under different cross-section.

Fig. 13 compare the time evolution of amplitude at $x=0$ and the distribution under different time with the theory value, under different cross-section. For both $\sigma=100$ and $\sigma=1000$ cases, the UGKP simulated results also show good agreements with the theory value. These results confirm the capability of the extended UGKP method for pure scattering cases.

6 Conclusion

This work extends the UGKP method to solve the frequency-dependent radiative system with both absorption/emission and scattering processes under the unstructured mesh.

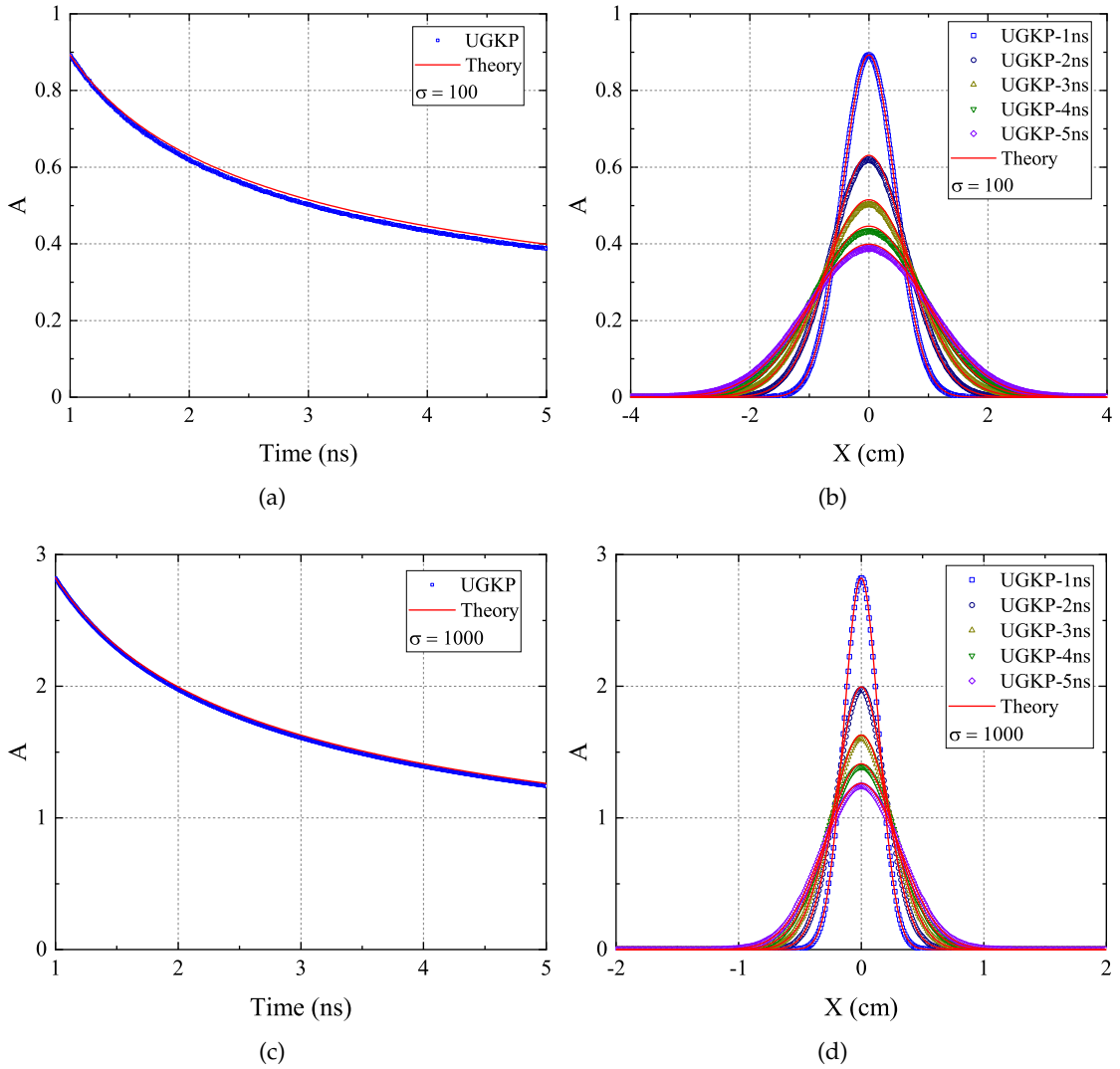

Figure 13: The time evolution of amplitude at $x=0$ for (a) $\sigma=100$, (c) $\sigma=1000$, and the distribution under different time for (b) $\sigma=100$, (d) $\sigma=1000$, compared with the theory value in (5.2).

The proposed UGKP method has the asymptotic preserving (AP) property in both optically thin and thick regimes for a continuum spectrum in the frequency domain. In addition, a smooth transition in the regime between the diffusion and free transport limit could be achieved by the extended UGKP method. Numerical simulation results are presented to verify the capability of the extended UGKP method and the code performance. The results of the one-dimensional Marshak wave problems and the two-dimensional Tophat problem confirm that the extended UGKP method captures the multiscale physical flow field in a wide range of regimes. The results of the sinusoidal and Gauss wave

diffusion problems prove the extended UGKP method for the pure scattering cases. The results of a self-designed multi-group problem verify the extended UGKP method for the frequency-dependent radiation cases, and the Marshak wave problems with the scattering effect verify the extended UGKP method for capturing both the absorption/emission and the scattering effect. The proposed UGKP for the multi-frequency radiative transfer problem shows advantages in the simulation of multiscale photon transport problems. The scheme and code will be applied in high-energy-density physics engineering applications.

Credit authorship contribution statement

Yuan Hu: Methodology, Software, Investigation, Writing – original draft. Chang Liu: Methodology, Software, Writing – review & editing, Supervision, Resources. Huayun Shen: Supervision, Resources. Shiyang Zou: Supervision, Resources. Baolin Tian: Supervision, Resources.

Acknowledgments

Chang Liu is partially supported by the National Key R&D Program of China (2022YFA1004500), the National Natural Science Foundation of China (12102061,12031001), the Presidential Foundation of the China Academy of Engineering Physics (YZJJZQ2022017), the Beijing Natural Science Foundation (Z230003). The authors are partially supported by the National Natural Science Foundation of China (12005020).

References

[1] Ke Lan. Dream fusion in octahedral spherical hohlraum. *Matter and Radiation at Extremes*, 7(5):055701, 2022.

[2] Yao-Hua Chen, Zhichao Li, Hui Cao, Kaiqiang Pan, Sanwei Li, Xufei Xie, Bo Deng, Qiangqiang Wang, Zhurong Cao, Lifei Hou, et al. Determination of laser entrance hole size for ignition-scale octahedral spherical hohlraums. *Matter and Radiation at Extremes*, 7(6):065901, 2022.

[3] Allan B Wollaber. Four decades of implicit Monte Carlo. *Journal of Computational and Theoretical Transport*, 45(1-2):1–70, 2016.

[4] Ulrich M Noebauer and Stuart A Sim. Monte Carlo radiative transfer. *Living Reviews in Computational Astrophysics*, 5:1–103, 2019.

[5] Martin Frank, Bruno Dubroca, and Axel Klar. Partial moment entropy approximation to radiative heat transfer. *Journal of Computational Physics*, 218(1):1–18, 2006.

[6] José A Carrillo, Thierry Goudon, Pauline Lafitte, and Francesco Vecil. Numerical schemes of diffusion asymptotics and moment closures for kinetic equations. *Journal of Scientific Computing*, 36:113–149, 2008.

[7] V Vikas, Cory D Hauck, Zhi Jian Wang, and Rodney O Fox. Radiation transport modeling using extended quadrature method of moments. *Journal of Computational Physics*, 246:221–241, 2013.
[8] Graham W Alldredge, Ruo Li, and Weiming Li. Approximating the M2 method by the extended quadrature method of moments for radiative transfer in slab geometry. *Kinetic & Related Models*, 9(2), 2016.
[9] Zhenning Cai, Ruo Li, and Yanli Wang. An efficient NRxx method for Boltzmann-BGK equation. *Journal of Scientific Computing*, 50:103–119, 2012.
[10] Zhengyi Li, Bin Dong, and Yanli Wang. Learning invariance preserving moment closure model for Boltzmann-BGK equation. *arXiv preprint arXiv:2110.03682*, 2021.
[11] Brian Hunter and Zhixiong Guo. Comparison of quadrature schemes in DOM for anisotropic scattering radiative transfer analysis. *Numerical Heat Transfer, Part B: Fundamentals*, 63(6):485–507, 2013.
[12] Pedro J Coelho. Advances in the discrete ordinates and finite volume methods for the solution of radiative heat transfer problems in participating media. *Journal of Quantitative Spectroscopy and Radiative Transfer*, 145:121–146, 2014.
[13] Shang-Shang Chen, Ben-Wen Li, and Ya-Song Sun. Chebyshev collocation spectral method for solving radiative transfer with the modified discrete ordinates formulations. *International Journal of Heat and Mass Transfer*, 88:388–397, 2015.
[14] TH Roos, TM Harms, and CG Du Toit. Conservation of scattered energy and asymmetry factor in the new rotationally symmetric spherical discretisation scheme. *International Journal of Heat and Mass Transfer*, 101:205–225, 2016.
[15] Luc Mieussens. Discrete velocity model and implicit scheme for the BGK equation of rarefied gas dynamics. *Mathematical Models and Methods in Applied Sciences*, 10(08):1121–1149, 2000.
[16] Jinxue Fu, Weiming Li, Peng Song, and Yanli Wang. An asymptotic-preserving IMEX method for nonlinear radiative transfer equation. *Journal of Scientific Computing*, 92(1):27, 2022.
[17] Joseph A Fleck Jr and JD Cummings Jr. An implicit Monte Carlo scheme for calculating time and frequency dependent nonlinear radiation transport. *Journal of Computational Physics*, 8(3):313–342, 1971.
[18] LB Lucy. Computing radiative equilibria with Monte Carlo techniques. *Astronomy and Astrophysics*, 344:282–288, 1999.
[19] Carole K Hayakawa, Jerome Spanier, and Vasan Venugopalan. Coupled forward-adjoint Monte Carlo simulations of radiative transport for the study of optical probe design in heterogeneous tissues. *SIAM Journal on Applied Mathematics*, 68(1):253–270, 2007.
[20] NA Gentile and Ben C Yee. Iterative implicit Monte Carlo. *Journal of Computational and Theoretical Transport*, 45(1-2):71–98, 2016.
[21] JA Fleck Jr and EH Canfield. A random walk procedure for improving the computational efficiency of the implicit Monte Carlo method for nonlinear radiation transport. *Journal of Computational Physics*, 54(3):508–523, 1984.
[22] J Giorla and R Sentis. A random walk method for solving radiative transfer equations. *Journal of Computational Physics*, 70(1):145–165, 1987.
[23] NA Gentile. Implicit Monte Carlo diffusion—an acceleration method for Monte Carlo time-dependent radiative transfer simulations. *Journal of Computational Physics*, 172(2):543–571, 2001.
[24] Jeffery D Densmore, Todd J Urbatsch, Thomas M Evans, and Michael W Buksas. A hy-

brid transport-diffusion method for Monte Carlo radiative-transfer simulations. *Journal of Computational Physics*, 222(2):485–503, 2007.

[25] Jeffery D Densmore, Kelly G Thompson, and Todd J Urbatsch. A hybrid transport-diffusion Monte Carlo method for frequency-dependent radiative-transfer simulations. *Journal of Computational Physics*, 231(20):6924–6934, 2012.

[26] H Park, DA Knoll, RM Rauenzahn, AB Wollaber, and JD Densmore. A consistent, moment-based, multiscale solution approach for thermal radiative transfer problems. *Transport Theory and Statistical Physics*, 41(3-4):284–303, 2012.

[27] H Park, Dana A Knoll, Rick M Rauenzahn, Christopher K Newman, JD Densmore, and AB3120767 Wollaber. An efficient and time accurate, moment-based scale-bridging algorithm for thermal radiative transfer problems. *SIAM Journal on Scientific Computing*, 35(5):S18–S41, 2013.

[28] JD Densmore, H Park, Allan B Wollaber, Rick M Rauenzahn, and Dana A Knoll. Monte Carlo simulation methods in moment-based scale-bridging algorithms for thermal radiative-transfer problems. *Journal of Computational Physics*, 284:40–58, 2015.

[29] Hans Hammer, HyeongKae Park, and Luis Chacon. A multi-dimensional, moment-accelerated deterministic particle method for time-dependent, multi-frequency thermal radiative transfer problems. *Journal of Computational Physics*, 386:653–674, 2019.

[30] H Park, Luis Chacón, Anna Matsekh, and Guangye Chen. A multigroup moment-accelerated deterministic particle solver for 1-D time-dependent thermal radiative transfer problems. *Journal of Computational Physics*, 388:416–438, 2019.

[31] Shi Jin. Efficient asymptotic-preserving (AP) schemes for some multiscale kinetic equations. *SIAM Journal of Scientific Computing*, 21:441—-454, 1999.

[32] Shi Jin. Asymptotic preserving (AP) schemes for multiscale kinetic and hyperbolic equations: A review. *Lecture Notes for Summer School on Methods and Models of Kinetic Theory (M&MKT), Porto Ercole (Grosseto, Italy)*, pages 177–216, 2010.

[33] Zhaoli Guo, Jiequan Li, and Kun Xu. Unified preserving properties of kinetic schemes. *Physical Review E*, 107(2):025301, 2023.

[34] Kun Xu and Juan-Chen Huang. A unified gas-kinetic scheme for continuum and rarefied flows. *Journal of Computational Physics*, 229(20):7747–7764, 2010.

[35] Luc Mieussens. On the asymptotic preserving property of the unified gas kinetic scheme for the diffusion limit of linear kinetic models. *Journal of Computational Physics*, 253:138–156, 2013.

[36] Wenjun Sun, Song Jiang, and Kun Xu. An asymptotic preserving unified gas kinetic scheme for gray radiative transfer equations. *Journal of Computational Physics*, 285:265–279, 2015.

[37] Wenjun Sun, Song Jiang, Kun Xu, and Shu Li. An asymptotic preserving unified gas kinetic scheme for frequency-dependent radiative transfer equations. *Journal of Computational Physics*, 302:222–238, 2015.

[38] Wenjun Sun, Song Jiang, and Kun Xu. An implicit unified gas kinetic scheme for radiative transfer with equilibrium and non-equilibrium diffusive limits. *Communications in Computational Physics*, 22(4):889–912, 2017.

[39] Wenjun Sun, Song Jiang, and Kun Xu. A multidimensional unified gas-kinetic scheme for radiative transfer equations on unstructured mesh. *Journal of Computational Physics*, 351:455–472, 2017.

[40] Wenjun Sun, Song Jiang, and Kun Xu. An asymptotic preserving implicit unified gas kinetic scheme for frequency-dependent radiative transfer equations. *International Journal of Numerical Analysis & Modeling*, 15, 2018.

[41] Yi Shi, Peng Song, and WenJun Sun. An asymptotic preserving unified gas kinetic particle method for radiative transfer equations. *Journal of Computational Physics*, 420:109687, 2020.
[42] Yi Shi, Wenjun Sun, Lingxiao Li, and Peng Song. An improved unified gas kinetic particle method for radiative transfer equations. *Journal of Quantitative Spectroscopy and Radiative Transfer*, 261:107428, 2021.
[43] Weiming Li, Chang Liu, Yajun Zhu, Jiwei Zhang, and Kun Xu. Unified gas-kinetic wave-particle methods III: Multiscale photon transport. *Journal of Computational Physics*, 408:109280, 2020.
[44] Pauline Godillon-Lafitte and Thierry Goudon. A coupled model for radiative transfer: Doppler effects, equilibrium, and nonequilibrium diffusion asymptotics. *Multiscale Modeling & Simulation*, 4(4):1245–1279, 2005.
[45] Christophe Buet and Bruno Despres. Asymptotic analysis of fluid models for the coupling of radiation and hydrodynamics. *Journal of Quantitative Spectroscopy and Radiative Transfer*, 85(3-4):385–418, 2004.
[46] Zhiqiang Sheng and Guangwei Yuan. A nine point scheme for the approximation of diffusion operators on distorted quadrilateral meshes. *SIAM Journal on Scientific Computing*, 30(3):1341–1361, 2008.
[47] Xiaojing Xu, Song Jiang, and Wenjun Sun. A positive and asymptotic preserving filtered PN method for the gray radiative transfer equations. *Journal of Computational Physics*, 444:110546, 2021.